


Variation in Coronal Activity from Solar Cycle 24 Minimum to Maximum Using Three-Dimensional Reconstructions of the Coronal Electron Density from STEREO/COR1

Tongjiang Wang^{1,2}  · Nelson L. Reginald^{1,2} · Joseph M. Davila² · O. Chris St. Cyr² · William T. Thompson³

Received: 8 March 2017 / Accepted: 19 June 2017 / Published online: 21 July 2017
© Springer Science+Business Media B.V. (outside the USA) 2017

Abstract Three-dimensional electron density distributions in the solar corona are reconstructed for 100 Carrington rotations (CR 2054–2153) during 2007/03–2014/08 using the spherically symmetric method from polarized white-light observations with the *inner coronagraph* (COR1) onboard the twin *Solar Terrestrial Relations Observatory* (STEREO). These three-dimensional electron density distributions are validated by comparison with similar density models derived using other methods such as tomography and a magnetohydrodynamics (MHD) model as well as using data from the *Solar and Heliospheric Observatory* (SOHO)/*Large Angle and Spectrometric Coronagraph* (LASCO)-C2. Uncertainties in the estimated total mass of the global corona are analyzed based on differences between the density distributions for COR1-A and -B. Long-term variations of coronal activity in terms of the global and hemispheric average electron densities (equivalent to the total coronal mass) reveal a hemispheric asymmetry during the rising phase of Solar Cycle 24, with the northern hemisphere leading the southern hemisphere by a phase shift of 7–9 months. Using 14 CR (\approx 13-month) running averages, the amplitudes of the variation in average electron density between Cycle 24 maximum and Cycle 23/24 minimum (called the modulation factors) are found to be in the range of 1.6–4.3. These modulation factors are latitudinally dependent, being largest in polar regions and smallest in the equatorial region. These modulation factors also show a hemispheric asymmetry: they are somewhat larger in the southern hemisphere. The wavelet analysis shows that the short-term quasi-periodic oscillations during the rising

Electronic supplementary material The online version of this article (doi:[10.1007/s11207-017-1130-3](https://doi.org/10.1007/s11207-017-1130-3)) contains supplementary material, which is available to authorized users.

✉ T. Wang
tongjiang.wang@nasa.gov
N.L. Reginald
nelson.l.reginald@nasa.gov

¹ Department of Physics, Catholic University of America, 620 Michigan Avenue NE, Washington, DC 20064, USA

² NASA Goddard Space Flight Center, Code 671, Greenbelt, MD 20771, USA

³ ADNET Systems, Inc., NASA Goddard Space Flight Center, Code 671, Greenbelt, MD 20771, USA

and maximum phases of Cycle 24 have a dominant period of 7–8 months. In addition, it is found that the radial distribution of the mean electron density for streamers at Cycle 24 maximum is only slightly larger (by $\approx 30\%$) than at cycle minimum.

Keywords Solar corona · Electron density · Solar cycle · Oscillations · STEREO · COR1

1. Introduction

The solar cycle is the long-term (≈ 11 -year) variation in solar activity, manifested in various phenomena such as sunspot numbers, flares, coronal mass ejections (CMEs), and total solar radiation (see Hathaway, 2015 for a review). It is a well-accepted fact that the solar cycle is virtually the magnetic cycle (with a full period of ≈ 22 years due to the 11-year polarity reversal of sunspots and polar fields) and is produced by dynamo processes within the Sun (see Charbonneau, 2010 for a review). At solar minimum, a dipolar field dominates the large-scale structure of the solar corona, and it is characterized by a long-lived helmet streamer belt and large polar coronal holes (CHs), whereas during solar maximum, higher-order components of the magnetic field strengthen, resulting in large-scale coronal structures that are increased in complexity (Linker *et al.*, 1999; Riley *et al.*, 2006; Hu *et al.*, 2008; Yeates and Muñoz Jaramillo, 2013). This is indicated by a widening of the streamer belt to higher latitudes and the emergence of pseudo- and polar streamers. The solar magnetic field is understood to play a crucial role in forming the structure of the solar corona and inner heliosphere (see Linker *et al.*, 1999 and Mackay and Yeates, 2012 for a review). However, direct measurements of the weak coronal magnetic field are still not possible. To obtain the global magnetic structure of the solar corona, we mainly rely on the simple potential field source surface (PFSS) model (Schatten, Wilcox, and Ness, 1969; Altschuler and Newkirk, 1969; Schrijver and De Rosa, 2003) and more advanced magnetohydrodynamics (MHD) models (Riley *et al.*, 2006; Hu *et al.*, 2008; Lionello, Linker, and Mikić, 2009; Rušin *et al.*, 2010). To validate these models, the calculated coronal magnetic structures are often compared with white-light observations of particular coronal brightness structures such as helmet streamers and coronal holes. This is because the coronal plasma outlines the direction of the magnetic field in the highly conducting solar corona where the plasma and magnetic field are effectively frozen together. As a result, systematic long-term observations of the coronal brightness structure should be able to reflect morphological and topological changes of the large-scale coronal magnetic field over the solar cycle. For example, using a three-dimensional (3D) MHD model with the observed line-of-sight (LOS) photospheric magnetic field as boundary conditions, Hu *et al.* (2008) studied the evolution of the heliospheric current sheet (HCS) and the coronal magnetic field configuration during Cycle 23, and confirmed the close spatial relationship between the observed white-light streamer structures and the HCS (*e.g.* Guhathakurta, Holzer, and MacQueen, 1996 and references therein).

The K-coronal brightness variation (and by inference, the variation in coronal mass) with solar cycle was first detected from eclipse observations, and was followed with systematic studies using long-term observations by ground- and space-based coronagraphs. For example, from inner coronal observations (at 1.3 and 1.5 R_{\odot} from the Sun center), Fisher and Sime (1984) deduced that the integrated polarized brightness (pB) of the K corona increased by a factor of 2 from the minimum to maximum during Cycles 20 and 21. They also found that the total coronal hole area increased from zero at solar maximum to a value of up to about one quarter of the global area at solar minimum. Using the outer coronal observations

(at $2.0\text{--}3.4 R_{\odot}$) from the *Solar Maximum Mission* (SMM) coronagraph during Solar Cycle 22, MacQueen *et al.* (2001) showed that the K-coronal brightness (or mass) varied by a factor of 4 between the solar maximum and minimum, and was closely correlated with the occurrence rate and average mass of CMEs. Using white-light observations from the *Large Angle and Spectrometric Coronagraph* (LASCO)-C2 on the *Solar and Heliospheric Observatory* (SOHO) spacecraft, Lamy *et al.* (2014) compared the solar activity minima of Cycles 22/23 and 23/24, and Barlyaeva, Lamy, and Llebaria (2015) studied the variability of the K-coronal radiance over timescales ranging from mid-term (0.6–4 years) quasi-periodicities to the long-term solar cycle. The mid-term quasi-periodicities appear to be a basic property of the solar activity. This was suggested by the fact that many features are common to different observations in the solar atmosphere and even in the convective zone (see Bazilevskaya *et al.*, 2014 for a review). In addition, the observed hemispheric asymmetry is another important property of the solar activity to be understood (Usoskin, Sokoloff, and Moss, 2009; McIntosh *et al.*, 2013; Bazilevskaya *et al.*, 2014; Richardson, von Roseninge, and Cane, 2016; Norton, Charbonneau, and Passos, 2014).

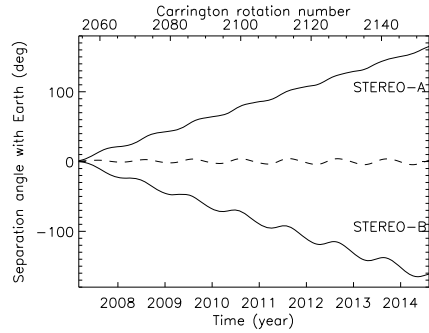
In this article, we present the variations in coronal activity during Solar Cycle 24 based on the 3D electron density distribution derived from pB observations of the K-corona using the *Sun Earth Connection Coronal and Heliospheric Investigation* (SECCHI)-*inner coronagraph* (COR1) telescopes (Thompson *et al.*, 2003; Thompson and Reginald, 2008) onboard the twin *Solar Terrestrial Relations Observatory* (STEREO) spacecraft (Howard *et al.*, 2008). In Section 2 we describe the method used to reconstruct the 3D electron density of the corona, and in Section 3 we validate the reconstructed density models using several techniques. In Section 4 we then analyze the hemispheric asymmetry and the short-period oscillations of the average electron density (or coronal mass) during the rising and maximum phases of Cycle 24, and the associated variations in the streamer area and electron density. In Section 5 we present the discussion and conclusions from our study.

2. 3D Electron Density Reconstructions Using STEREO/COR1

We reconstructed 3D distributions of the coronal electron density for 100 Carrington rotations (CRs) from CR 2054 to CR 2153 using the pB data acquired by STEREO/COR1. During this period, both STEREO spacecraft ran in the heliocentric orbit that is close to the Earth's. Spacecraft-A (Ahead) drifts away from Earth in the direction of the Earth's rotation with an orbital period slightly shorter than a year, while spacecraft-B (Behind) drifts away from Earth in the opposite direction with an orbital period slightly longer than a year. The two spacecraft separate from each other at an average rate of approximately 45° per year. Figure 1 shows that STEREO-A and STEREO-B were separated from the Earth by between $1.2^{\circ}\text{--}165.9^{\circ}$ and $0.2^{\circ}\text{--}160.9^{\circ}$, respectively, during the period of interest, *i.e.* from 04:14 UT on 4 March 2007 (the beginning time of CR 2054 viewed from Earth) to 11:05 UT on 21 August 2014 (the ending time of CR 2153). COR1 observes the white-light K corona from about 1.4 to $4 R_{\odot}$ in a waveband of 22.5 nm width centered on the H α line at 656 nm. The data are taken with a cadence of 10 minutes and are transmitted in the binning format of 1024×1024 from the spacecraft. Since 19 April 2009, the normal cadence is increased to 5 minutes and the binned images are in the 512×512 format. The instrumental scattered light in the pB data is removed by subtracting the combined monthly minimum and calibration roll backgrounds (Thompson *et al.*, 2010).

We used the spherically symmetric polynomial approximation (SSPA) method to reconstruct the 3D coronal density. The SSPA method is based on the assumption that the radial

Figure 1 Separation angles of the STEREO-A/B spacecraft with the Earth during the period from 2007/03/04 to 2014/08/07. The positive and negative values indicate STEREO-A and -B, respectively. The *dashed line* indicates the median position of the separation angle between the two spacecraft relative to Earth.



electron density distribution has the polynomial form, $N(r) = \sum_k a_k r^{-k}$, where r is the radial distance from the Sun center, k is the degree of the polynomial, and a_k are unknown coefficients (Hayes, Vourlidas, and Howard, 2001; Wang and Davila, 2014). The coefficients a_k can be determined by a multivariate least-squares fit to the radial profile of pB data. Wang and Davila (2014) validated the SSPA method using synthesized pB images from a 3D density model reconstructed by tomography from COR1 observations, and showed that the derived density is consistent with model inputs in the plane of the sky (POS) generally within a factor of two. The degree of $k = 5$ is typically suitable for COR1 pB inversion. In addition, Wang and Davila (2014) also demonstrated a reconstruction of the 3D coronal density using the SSPA method. Here we adopted a similar procedure as described below.

Each reconstruction was made of 2D density maps ($N(r, \theta)$) with the radial and latitudinal dependence in the POS. These 2D density maps were inverted by the SSPA method from a set of pB data (typically including 56 images with a cadence of 6 hours, which corresponds to a longitudinal step of about 3°) over a period of 13.6 days. Thus, two reconstructions were made for a given CR. If an image at some sampled time was missing or bad, it was replaced with the one observed closest to that time. First, a 2D density map was derived by fitting the radial pB data between 1.6 and $3.7 R_\odot$ using the SSPA inversion at 120 angular positions (with intervals of 3°) surrounding the Sun for each image. Then the east-limb and west-limb density profiles of all the images were mapped into spherical cross-sections at different heights (with an interval of $0.1 R_\odot$) based on their Carrington coordinates. After converting the irregular grid into the regular grid ($2^\circ \times 2^\circ$ in longitude and latitude), a 3D density reconstruction in the radial range of $1.5 - 3.7 R_\odot$ was finally obtained.

By applying this method to STEREO/COR1 pB observations during 2007–2014, we obtained 200 reconstructions of the 3D coronal density for CRs 2054–2153 from COR1-A and COR1-B, respectively. We averaged the reconstructions for COR1-A and -B and constructed a $10^\circ \times 10^\circ$ smoothed coronal density map to compare with coronal density models determined by other methods (see Section 3). Figure 2 shows two examples, one for CR 2072 for the period of 20 July–3 August 2008 during solar minimum, the other for CR 2120 for the period of 6–19 February 2012 during solar maximum. An animation showing all density reconstructions at $2 R_\odot$ for CRs 2054–2153 from COR1-A and -B as well as their average is available in the online version of the journal.

3. Validations

In the following sections we compare our reconstructed 3D distributions of the coronal electron density with several different techniques. These include the derivation based on

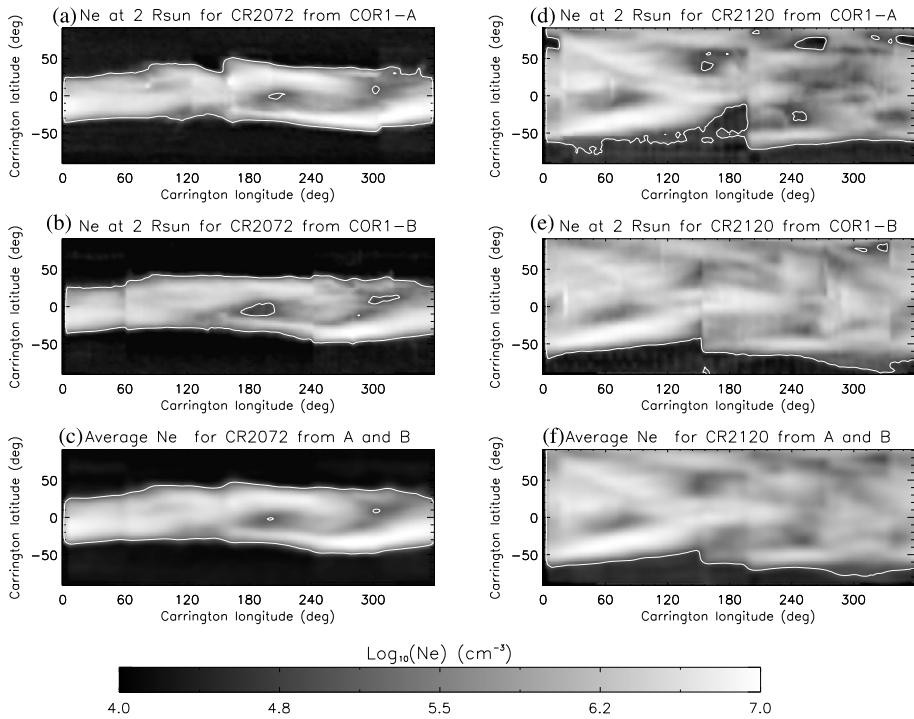


Figure 2 Two examples of the 3D coronal electron density reconstructed by the SSPA method. *Left panels:* for CR 2072 during solar minimum, showing a spherical cross-section of the density at $2.0 R_{\odot}$ from COR1-A (*top*), COR1-B (*middle*), and the mean of COR1-A and -B with $10^{\circ} \times 10^{\circ}$ smoothing (*bottom*). *Right panels:* same as the left panels, but for CR 2120 during solar maximum. The overlaid contour encloses regions with density $N_e > 3\sigma$ (see Figure 15). An animation of 200 reconstructions for CRs 2054–2153 during 2007–2014 is available in the online version of the journal.

LASCO C2, tomographic reconstruction, and MHD modeling. We also analyze the sources of uncertainty in our estimated total coronal mass for these reconstructions.

3.1. LASCO/C2 pB Inversion

SOHO/LASCO-C2 has typically made one pB sequence per day since late 1995 (Brueckner *et al.*, 1995). The C2 has an effective field of view (FOV) of $2.2 - 6.1 R_{\odot}$ (Frazin *et al.*, 2012), and overlaps with that of STEREO/COR1. This allows us to use the 2D coronal density $N(r, \theta)$ inverted from the C2 pB images to validate the reconstructed 3D coronal density from COR1. Since the 3D density of COR1 is essentially made using the sequence of 2D density maps, comparisons with the 2D density of COR2 cannot provide direct examination of 3D characteristics of the corona, but may allow us to test the requirement that main coronal structures need to be stable over about two weeks for reconstruction. This is because the 3D density reconstructions presented here are the average between COR1-A and COR1-B, and the 2D density distributions used for comparison between COR1-A/B and C2 in the same POS (*i.e.* when viewed from the same direction in the Carrington coordinate system) are observed at different times (see the following examples).

We used the calibrated C2 pB images that are available in the NRL archive.¹ We chose the 3D density reconstructions for CR 2072 and CR 2120 as examples (see Figure 2). We used the routine `PB_INVERTER` in SolarSoftWare (SSW; see Freeland and Handy, 1998) to derive the 2D coronal density distribution from the C2 pB images. This routine uses the Van de Hulst (VdH) technique (Van de Hulst, 1950). In the VdH inversion the radial distribution of pB in the POS is assumed to follow a polynomial function, while in the SSPA inversion the electron density distribution is assumed to follow a polynomial function. Wang and Davila (2014) showed in theory and observation that these two methods are equivalent. We modified the code `PB_INVERTER` by replacing the use of the IDL function `CURVEFIT` with `SVDFIT` in fitting the radial pB data to a polynomial function with the degree k equal to four, because the `SVDFIT` works better in the case of computing a linear least-squares fit. Figures 3a and 3b show the density maps derived from the C2 pB images observed at 10:00 UT on 1 August 2008 during solar minimum and at about 03:00 UT on 10 February 2012 during solar maximum, respectively. For comparison we constructed the 2D density maps from the COR1 3D density model by calculating its cross-sectional distribution at the POS as viewed from Earth at the observing time for LASCO/C2 images. Figure 3c shows a density map from CR 2072 that is equivalent to the average between $N(r, \theta)$ obtained from COR1-A at 2008/07/21 09:00 UT and that of COR1-B at 2008/07/30 06:00 UT. Figure 3d shows an equivalent average between the density maps from COR1-A at 2012/02/18 9:00 UT and from COR1-B at 2012/02/15 00:00 UT for CR 2120. The 2D density distributions from COR1 and LASCO/C2 are found to be consistent. For quantitative comparison, we plot the COR1 and C2 density profiles as a function of position angles at two heights (2.5 and 3.0 R_{\odot}) in Figure 4. The comparison indicates a good coincidence in position and width between streamers in the COR1 and C2 density maps for solar minimum and maximum cases. The differences in the peak density are within a factor of two, comparable to the uncertainty from the SSPA inversion process (Wang and Davila, 2014).

3.2. Validation with Tomography

The tomographic technique reconstructs optically thin 3D coronal density structures using observations from multiple viewing directions, or using observations gathered over a period of half a solar rotation by a single spacecraft or only from Earth-based coronagraphs (*e.g.* Frazin and Janzen, 2002; Frazin *et al.*, 2007; Frazin *et al.*, 2010; Kramar *et al.*, 2009; Barbey, Guennou, and Auchère, 2013; Vibert *et al.*, 2016). Generally, only structures that are stable over about two weeks can be reliably reconstructed with tomographic techniques. Kramar *et al.* (2009) reconstructed a 3D coronal electron density model for CR 2066 for the period of 1–14 February 2008 based on 28 pB images (with a cadence of about two images per day) from COR1-B using the regularized tomographic inversion method. Wang and Davila (2014) compared this tomographic reconstruction with the SSPA reconstruction based on the same dataset, and found them to be consistent. The ratios of the tomographic density to the SSPA density in the streamer belt are very close to 1, typically in the range 1/2–2. Here we reconstructed the SSPA 3D coronal density for the same period, but consisting of 55 pB images (about four images per day) from COR1-A and -B. The mean density distributions for COR1-A and -B show a good agreement with those by tomography obtained with 28 pB images at different heliocentric distances (see Figure 5). pB data with higher cadence do not help to improve the actual spatial resolution of the reconstructed density in longitude because the SSPA method has an intrinsic limitation (with angular resolution of $\approx 50^\circ$) in

¹<http://lasco-www.nrl.navy.mil/content/retrieve/polarize/>

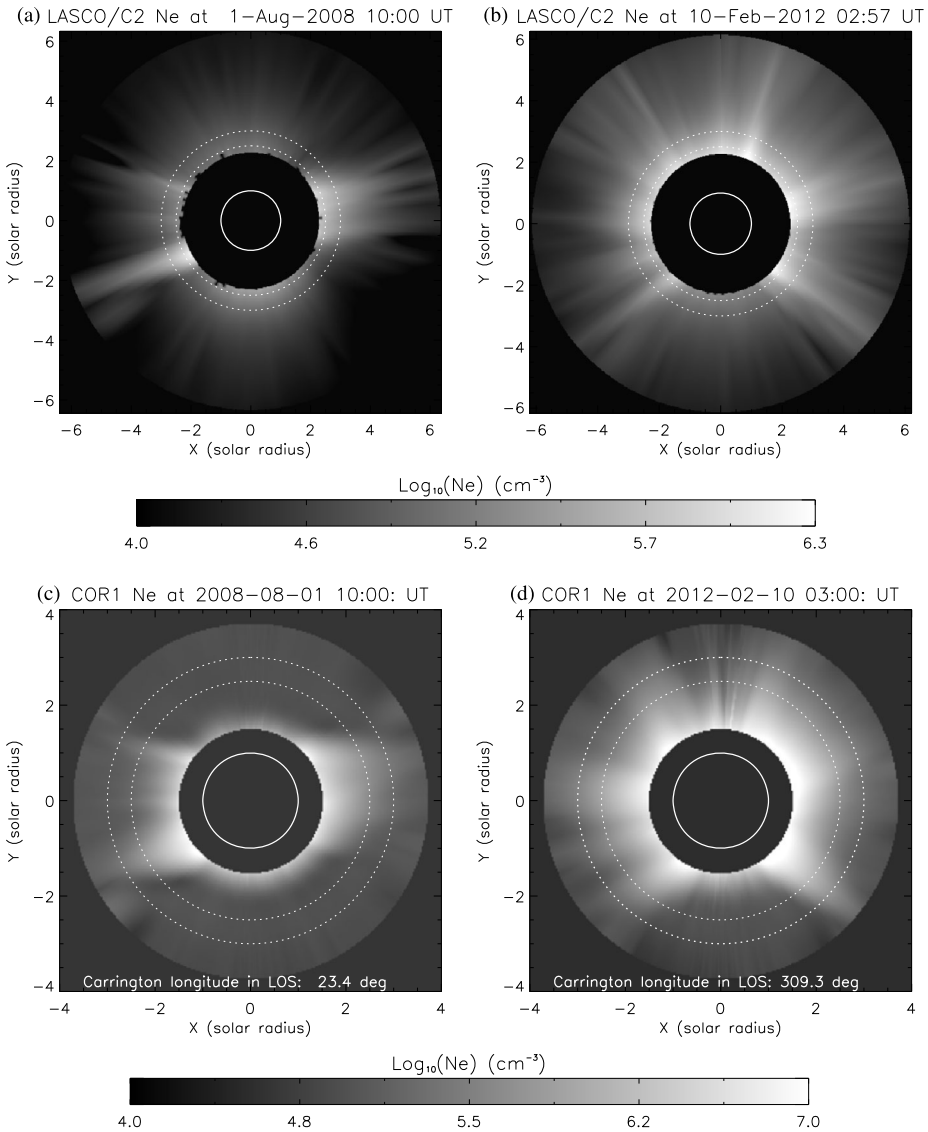


Figure 3 Comparison between the STEREO/COR1 and LASCO/C2 coronal densities. (a) and (b): 2D electron density maps derived by Van de Hulst (VdH) inversion from LASCO/C2 pB images observed at 10:00 UT on 1 August 2008 and at 02:57 UT on 10 February 2012, respectively. (c) and (d): cross sections of the STEREO/COR1 3D electron density at the POS, corresponding to positions of the Earth at the LASCO observing times in (a) and (b), respectively. In (c) and (d) the 3D coronal density for CR 2072 and CR 2120 is used, respectively, and the Carrington longitude of the LOS direction (23.4° in (c) and 309.3° in (d)) is marked at the bottom. In each panel the solid circle indicates the solar limb, and the two dotted circles (at 2.5 and $3.0 R_\odot$) mark the paths along which the density profiles are shown in Figure 4.

resolving the coronal structure near the POS. This is a result of the spherically symmetric approximation in inversion (Wang and Davila, 2014).

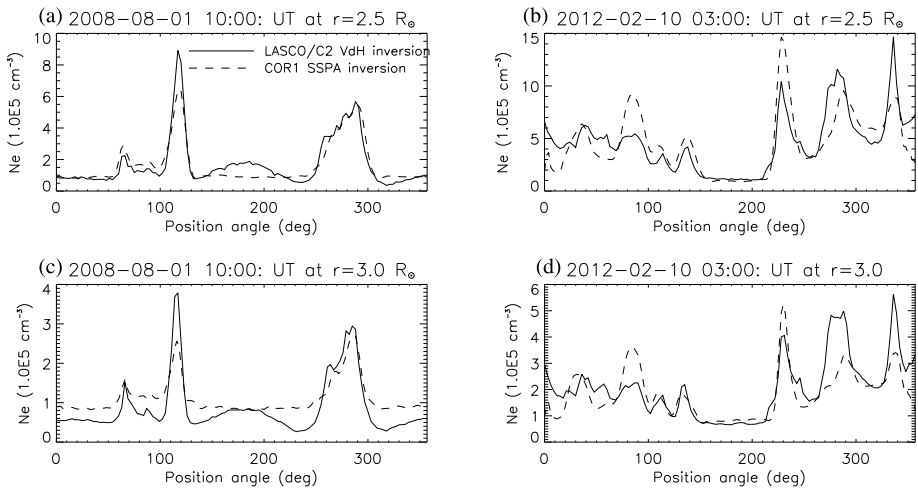


Figure 4 Comparison between the electron densities along two circular paths at $2.5 R_{\odot}$ (a)–(b), and $3.0 R_{\odot}$ (c)–(d) from the LASCO/C2 and STEREO/COR1 2D density maps. The position angle is counted anticlockwise from the North Pole. Panels (a) and (c) correspond to the case where LASCO/C2 data are observed at 10:00 UT on 1 August 2008, and panels (b) and (d) where LASCO/C2 data are observed at about 03:00 UT on 10 February 2012. In each panel the *solid line* represents the densities from the LASCO/C2 VdH inversion, and the *dashed line* represents the densities from the STEREO/COR1 SSPA inversion.

In addition, it is particularly useful to compare the globally averaged radial density profiles between the SSPA and tomography reconstructions because it helps to determine whether their coronal mass distributions are consistent overall in the analyzed volume despite the local difference. Figure 6 shows that the globally averaged density profile for tomography is consistent with the SSPA for COR1 within $1.8–3.7 R_{\odot}$. The better consistency with COR1-B than COR1-A is achieved because the tomographic reconstruction is made from the COR1-B data. It is estimated that the radial density for COR1-A is higher (by a factor of about 1.6) than for COR1-B in the outer part of the FOV ($2.7–3.7 R_{\odot}$). This difference may be explained by the fact that the COR1-B instrumental background is substantially lower than COR1-A before 30 January 2009. After that date, the level of scattering in COR1-A and -B becomes comparable (see Figure 8), likely as a result of contamination of the COR1-B objective by a dust particle (see the discussion in Section 3.4 and in Thompson *et al.*, 2010). In addition, the tomographic reconstruction used here may underestimate the density near the occulter by a factor of about 2–3 because of the boundary effect since the solution at the grid points close to the occulter is less well constrained by the observational data.

3.3. Validation with the MHD Simulation

In this section we show an example of validating the SSPA reconstruction with the MHD simulated coronal model. We used the Corona Heliosphere (CORHEL) and Magnetohydrodynamics Around a Sphere (MAS) model (known as the CORHEL MAS model) developed by Predictive Science Inc. (see Mikić *et al.*, 1999 for the details). The CORHEL MAS model is a sophisticated global thermodynamic MHD model that uses an improved equation for energy transport in the corona that includes parameterized coronal heating, parallel thermal conduction along the magnetic field lines, radiative losses, and acceleration by Alfvén waves

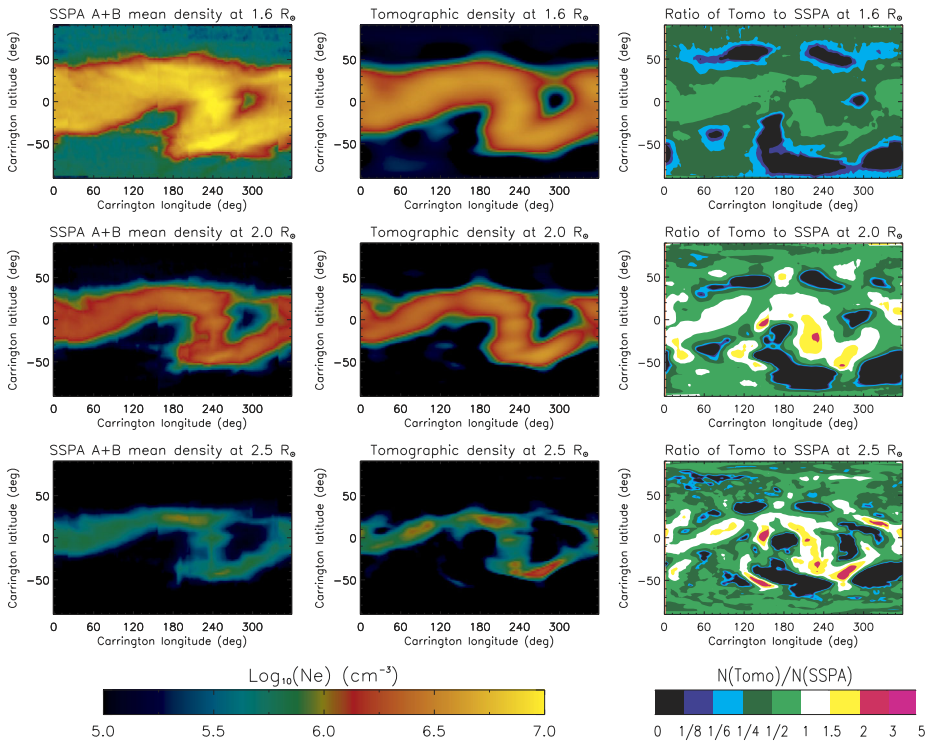
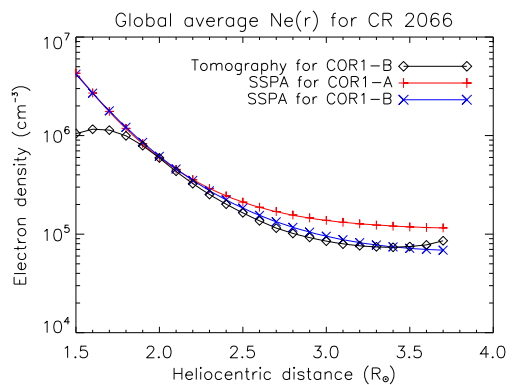


Figure 5 Comparison between the 3D coronal electron densities for CR 2066 reconstructed by SSPA and tomography methods. *Left panels:* spherical cross sections of the SSPA mean density for COR1-A and -B at 1.6, 2.0, and 2.5 R_{\odot} (from top to bottom). *Middle panels:* same as the left panels, but for the density reconstructed by tomography from COR1-B. *Right panels:* the ratio of the tomographic density (*second column*) to SSPA density (*first column*).

Figure 6 Radial profiles of the globally averaged coronal density for the SSPA and tomographic reconstructions for CR 2066. The values determined by tomography from COR1-B are shown with *diamonds*, and those by SSPA from COR1-A and COR1-B are shown with *pluses* and *crosses*, respectively.



(Mikić *et al.*, 2007). The global plasma density and temperature structures simulated by this model are capable of reproducing major coronal features observed in extreme ultraviolet (EUV) and X-ray emission, and they have been successfully used to predict the white-light

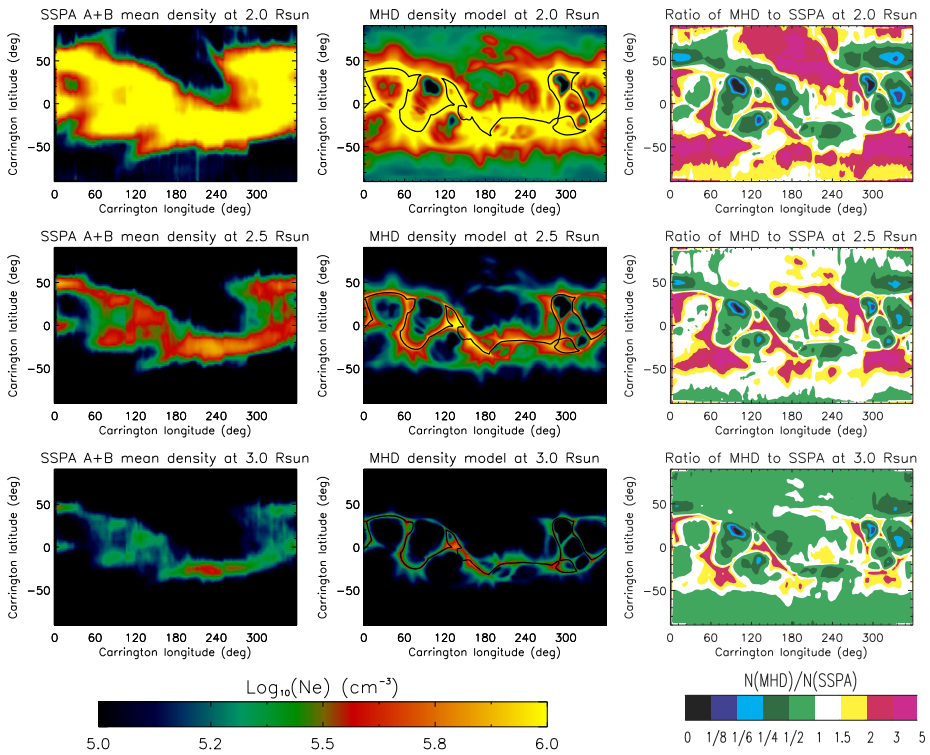


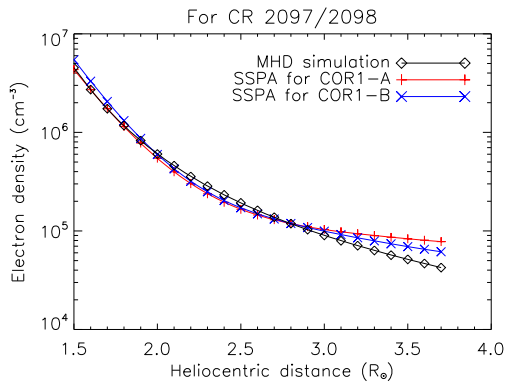
Figure 7 Comparison between the 3D coronal electron densities for CR2097/2098 derived by the SSPA inversion and MHD simulation. *Left panels:* spherical cross sections of the SSPA mean density from COR1-A and -B at 2.0, 2.5, and 3.0 R_{\odot} (from top to bottom). *Middle panels:* same as the left panels, but for the electron density from a MHD simulation of the solar eclipse of 11 July 2010 using SOHO/MDI magnetic field data. The *overlaid solid lines* denote the magnetic neutral line. *Right panels:* the ratio of the MHD simulated density (*second column*) to SSPA density (*first column*).

coronal structures for many total solar eclipses (*e.g.* Lionello, Linker, and Mikić, 2009; Rušin *et al.*, 2010).

The middle panels of Figure 7 show the modeled electron density at heliocentric distances of 2.0, 2.5, and 3.0 R_{\odot} from a thermodynamic MHD simulation. This simulation was carried out to predict the coronal structure of the 11 July 2010 eclipse, which used the photospheric magnetic field data measured with SOHO/MDI during a period from 10 June to 4 July 2010 (a combination of CR 2097 and 2098) as boundary conditions. The artificial data produced based on the simulated results were also used to test the tomography method (Kramar *et al.*, 2014) and to estimate uncertainties of the spherically symmetric model (SSM) in determining the electron temperatures and bulk flow speeds in the low corona (Reginald *et al.*, 2014).

To compare with the MHD simulated coronal density, we made two SSPA reconstructions for the period of 9 June–7 July 2010 using 111 pB images from COR1-A and -B, and then averaged them to obtain a mean density model. The left panels of Figure 7 show the electron density distributions at 2.0, 2.5, and 3.0 R_{\odot} from the SSPA density model. We find that the streamer regions with high densities are mainly located along the magnetic neutral lines. The SSPA and simulated density distributions are consistent overall, but the simulated

Figure 8 Comparison between the radial profiles of globally averaged electron density from the 3D distributions by SSPA and the MHD model. The values from the MHD model are shown with *diamonds*, and those from the SSPA COR1-A and COR1-B are shown with *pluses* and *crosses*, respectively.



density has more fine structures (see middle panels of Figure 7). Figure 8 compares the globally averaged radial density profiles in the range 1.5–3.7 R_⊙. The SSPA densities for both COR1-A and -B are consistent with the simulated results except for the region close to the outer part (> 3.5 R_⊙) of the COR1 FOV where the SSPA density values are slightly higher. This is probably because the pB data in that region have weak signal-to-noise ratios, leading to an inverted density signal just above the background noise level (see Figure 17b in Section 4.2).

The median position between STEREO-A and -B in heliographic longitude varies around the Earth with amplitudes smaller than 4° (see the dashed curve in Figure 1). This may account for the reasonable comparison between the SSPA density model obtained by averaging COR1-A and -B reconstructions and the model calculated from the MHD simulation using the SOHO/MDI magnetic field data.

3.4. Error Analysis

The reconstructions of the 3D coronal electron density from STEREO/COR1 are subject to several sources of uncertainties and error, including i) the effect of CMEs or other transient phenomena (e.g. coronal dimmings), ii) the temporal evolution of coronal structures within a given period, iii) the instrumental background subtraction, and iv) the spherically symmetric approximation in the SSPA inversion.

We first choose CR 2136, a density reconstruction during the maximum period of solar activity, as an example to detail the method of error analysis, then we show the results for the uncertainties for all rotations. Figure 9 shows the coronal mass distributions of CR 2136 for COR1-A and -B, which were calculated by integrating the 3D density in the region of 1.5–3.7 R_⊙ using

$$M(i, j) = \mu m_p R_\odot^3 \Delta\phi \Delta\theta \Delta r \sum_k N(i, j, k) r_k^2 \cos\theta_j, \tag{1}$$

where the electron density is assumed to be equal to the ion density, m_p is the mass of the proton, $\mu = 1.2$ is the mean molecular weight in the corona, $N(i, j, k)$ is the electron density value at a grid point (i, j, k) , $\Delta\phi$, $\Delta\theta$, Δr are the grid size in longitude, latitude, and radius, respectively, r_k is the dimensionless radial distance, and θ_j is the latitude. For a 3D density reconstruction, $\Delta\phi = \Delta\theta = 2^\circ (\pi/180^\circ)$ rad, $\Delta r = 0.1$, $r_k = [1.5, 3.7]$, and $\theta_j = [-90^\circ, 90^\circ]$. We calculate the total coronal mass for CR 2136 (and other rotations; see

Figure 9 Radially integrated coronal mass distributions of CR 2136 for the period of 1–15 May 2013 from COR1-A (a) and COR1-B (b). The vertical solid bars indicate the location and latitudinal width of CMEs that are listed in Table 1. An animation for CRs 2054–2153 is available in the online journal.

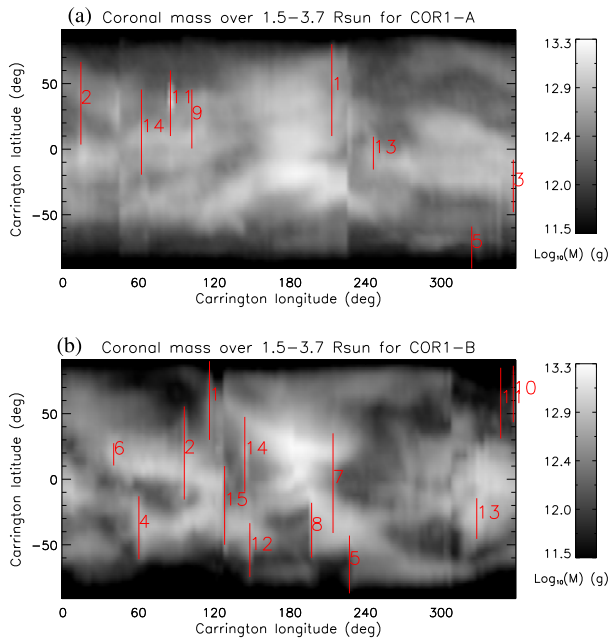


Figure 11a) by integrating the global corona:

$$M_{\text{total}} = \sum_{i,j} M(i, j). \tag{2}$$

We identify 15 CMEs from the pB images used for the reconstruction of CR 2136 based on the GSFSC COR1 CME catalog²; they are marked in Figure 9. Table 1 lists the observing time, Carrington coordinate of the center position (L_c , B_c), and latitudinal width (W) of these CMEs. Since the 3D density reconstruction was made with the pB images with a cadence of about 6 hours, each CME was detected in only one frame, but may cover 2–3 grid points in longitude because the reconstruction was regridded. We define Q as the longitudinal extent of the region influenced by CMEs. These CMEs are typically observed as a brightening in the mass distribution map (*e.g.* No. 11 for COR1-A and No. 2 for COR1-B), but sometimes CMEs also cause the destruction of large coronal structures, forming a long-lived coronal dimming (*e.g.* No. 5 and 8 for COR1-B). We estimated the change in coronal mass (M_{CME}) caused by a CME by integrating the mass distribution over a region of size $Q \times W$ centered at the location (L_c , B_c) by first removing the mass profile derived from the pB data observed immediately before the CME (see the pre-CME time t_{preCME} in Table 1). Here $Q = 6$ degrees (*i.e.* covering three grid points in longitude) was assumed. The obtained values of M_{CME} are found to lie in the range from -3×10^{13} g to 4×10^{14} g (see Table 1), where the positive and negative signs correspond to mass increase and decrease, respectively. When we take these CME-caused mass changes as errors for the total coronal mass ($M_{\text{total}} \approx 7 \times 10^{16}$ g) calculated for CR 2136 using Equation 2, we derive a total error of only 0.20% for COR1-A and 0.67% for COR1-B. This result suggests that the uncertainty caused by CMEs in measurements of the total coronal mass

²<https://cor1.gsfc.nasa.gov/catalog>

Table 1 CMEs observed in the COR1 pB images that were used for the 3D density reconstruction of CR 2136 during the period 1–15 May 2013^a.

CME No.	COR1-A					COR1-B						
	t_{CME} (UT)	t_{preCME} (UT)	L_c (deg)	B_c (deg)	W (deg)	M_{CME} (10^{12} g)	t_{CME} (UT)	t_{preCME} (UT)	L_c (deg)	B_c (deg)	W (deg)	M_{CME} (10^{12} g)
1	0502 06:00	0502 05:00	213	45	70	6.3	0502 06:00	0502 05:00	116	60	60	22.4
2	0503 18:00	0503 17:35	14	35	63	52.7	0503 18:00	0503 17:35	96	20	71	83.8
3	0505 00:05	0504 23:10	357	-28	40	23.0	not seen					
4	not seen						0506 11:55	0506 10:05	60	-37	48	-4.3
5	0507 12:00	0507 09:20	324	-75	32	-6.5	0507 11:55	0507 09:15	227	-65	44	-3.9
6	not seen						0508 00:05	0507 22:45	40	19	17	7.5
7	not seen						0508 12:00	0508 10:50	214	-3	76	412.8
8	not seen						0509 18:00	0509 17:10	197	-39	42	6.4
9	0510 17:55	0510 16:55	102	23	45	45.5	not seen					
10	not seen						0511 06:00	0510 23:30	357	65	43	-33.0
11	0512 00:05	0511 22:25	85	35	50	115.9	0512 00:05	0511 22:25	347	58	54	6.8
12	not seen						0513 12:00	0513 06:00	148	-54	41	48.8
13	0513 12:00	0513 07:25	246	-3	25	37.1	0513 12:00	0513 04:00	328	-30	31	43.4
14	0513 18:00	0513 17:10	62	13	65	53.3	0513 18:00	0513 17:10	144	19	57	62.7
15	not seen						0515 00:05	0514 22:35	128	-20	60	111.2

^a t_{CME} is the observing time of the pB images that capture a CME. t_{preCME} is the observing time of the pB images immediately previous to the CME. L_c and B_c are the Carrington longitude and latitude of the CME center position. W is the latitudinal width of the CMEs, and M_{CME} is the CME-caused coronal mass change.

from COR1 is negligible. The reason could lie in the fact that most of the CMEs (with the mass they carry) originate in the low corona below $1.5 R_{\odot}$ (e.g. Wang *et al.*, 2002; Gibson *et al.*, 2006). Our suggestion is also supported by the recent study by López *et al.* (2017), who estimated both the CME mass and the low-corona evacuated mass for three CMEs and found them both to be on the order of 10^{15} g, with the latter explaining a large fraction of the former. However, sometimes when a CME blows out streamers (e.g. CME No. 8 for COR1-B as the result of a large filament eruption) or if the streamer itself erupts to become a CME (e.g. No. 5 and 10 for COR1-B), then the resulting mass loss of the corona could be large. Kramar *et al.* (2011) analyzed such an event based on tomographic reconstructions of the 3D electron density in the corona before and after the CME using COR1 data and found a mass loss of $\approx 1.0 \times 10^{15}$ g.

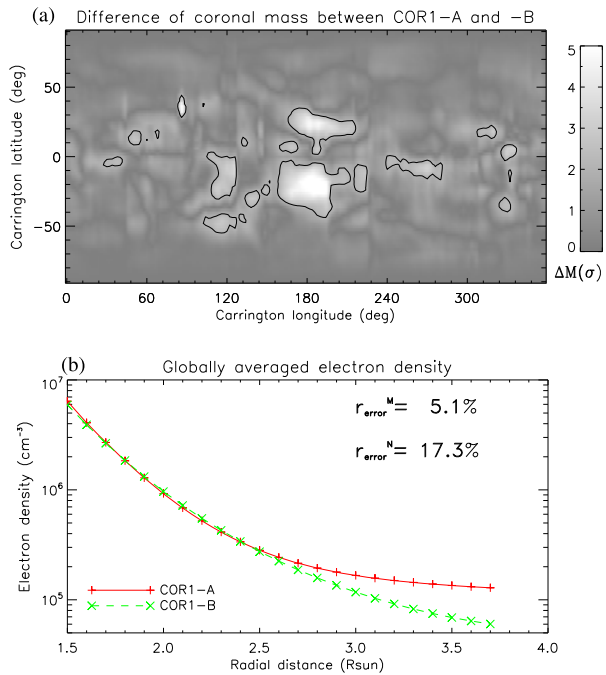
Since COR1-A and COR1-B generally observe the same coronal structure at different times (except when their separation is close to 0° or 180°), we may estimate errors of the coronal mass that are due to temporal evolution (including destruction of streamers) based on the difference of the mass distributions between COR1-A and COR1-B. As an example, we consider the 3D density reconstruction for CR 2136. Figure 9 shows that COR1-B observed a dimming region (at Carrington longitude from 160° to 195° and latitude from -60° to -20°) following CME No. 8 (see panel (b)), while COR1-A observed the pre-erupted coronal structure about six days before the CME (because the separation between COR1-A and -B was 83°). Thus the mass loss in the dimming region can be calculated from the difference of mass distributions between COR1-A and COR1-B. This example also implies that when we use the mean mass distribution between COR1-A and -B, the errors due to temporal evolution can be reduced by $\approx 50\%$. To be more general, we define “significant changes” in the mass distribution that are due to temporal evolution as unsigned mass differences between COR1-A and -B above 2σ . The σ here is the standard error for the average of $\Delta M(i, j) = M_A(i, j) - M_B(i, j)$, where $M_A(i, j)$ and $M_B(i, j)$ are the mass distributions for COR1-A and -B, respectively, obtained using Equation 1. Figure 10a shows the regions (S) with significant mass change (enclosed with the contour) for CR 2136 that cover the dimming region mentioned above. By taking the total unsigned difference within region S as an estimate of uncertainty in the total coronal mass caused by temporal evolution, we derive the relative error $r_{\text{error}}^M \approx 5\%$ for this reconstruction using the expression

$$r_{\text{error}}^M = \frac{\sum_{i,j \in S} |M_A(i, j) - M_B(i, j)|}{M_A + M_B} \quad (S = S(|\Delta M(i, j)| > 2\sigma)), \quad (3)$$

where M_A and M_B are the total coronal mass for COR1-A and -B calculated using Equation 2. With this method we estimated the errors for the 3D density reconstructions of CRs 2054–2153 (see the red line with pluses in Figure 11b), and found that $r_{\text{error}}^M = 1 - 10\%$ with mean values of 3.4% and 5.1% during the minimum phase and the maximum phase, respectively.

In addition, we compared the radial dependence of globally averaged electron densities between COR1-A and -B for CR 2136 (see Figure 10b), and found that they are consistent over the lower ($1.5 - 2.6 R_{\odot}$) region of high density, while their difference becomes distinct at the higher region close to the outer boundary of the FOV where the signals are weak. This feature suggests that the instrumental background noise may be an important source for uncertainty in the low-density region. To estimate the error for the globally averaged radial density distribution, we calculated the root mean square of the normalized density

Figure 10 (a) Mass difference map calculated between COR1-A and -B reconstructions of CR 2136 for the period of 1–15 May 2013. The color bar is in units of the standard error (σ) for the global average. The overlaid contour encloses regions of the mass difference with $|\Delta M(i, j)| > 2\sigma$. (b) Comparison of the radial profiles of the globally averaged coronal density for COR1-A and -B. The marked r_{error}^M and r_{error}^N are the errors for the total coronal mass and the average density calculated using Equations 3 and 4, respectively. An animation for CRs 2054–2153 is available in the online journal.



difference between COR1-A and -B using

$$r_{\text{error}}^N = \sqrt{\frac{1}{n} \sum_{k=1}^n \left(\frac{N_A(r_k) - N_B(r_k)}{N_A(r_k) + N_B(r_k)} \right)^2}, \tag{4}$$

where $N_A(r_k)$ and $N_B(r_k)$ are the globally averaged radial density profiles for COR1-A and -B, respectively, and $n = 23$ is the total number of radial grid points. We obtain $r_{\text{error}}^N \approx 17\%$ for CR 2136. For the 3D reconstructions of CRs 2054–2153, we find that $r_{\text{error}}^N = 3–26\%$ with mean values of 14% and 16% during the minimum and maximum phases, respectively (see the green line with crosses in Figure 11b). We also find that except for the period from 2008 to 2009 and at several peaks of r_{error}^M (e.g. in early 2010 and early 2012), the errors r_{error}^N and r_{error}^M vary with time with roughly the same trend. Notably the r_{error}^N drops about 50% after January 2009. This is most likely due to the serious dust deposition event on 30 January 2009 that led to an increase in the COR1-B background from a previously much lower level to that comparable to COR1-A (Thompson *et al.*, 2010).

The subtraction of the instrumental stray-light background is an important step in the COR1 calibration. The routine SECCHI_PREP in SSW processes COR1 images with a choice of two types of background images: the regular monthly minimum backgrounds (by default) or the combined backgrounds from both monthly minimum and calibration roll images (with the keyword /CALROLL) (see Thompson *et al.*, 2010 for details). The purpose of calibration rolls is to improve the background images by rejecting the residual K-coronal light from persistent streamers (mostly in the equatorial regions). Here, we applied the combined backgrounds to all pB images used in the density reconstructions. In the following, we analyze the uncertainty caused by the background subtraction based on differences between the total coronal masses from COR1-A and -B. Figure 11b shows that the relative mass differences

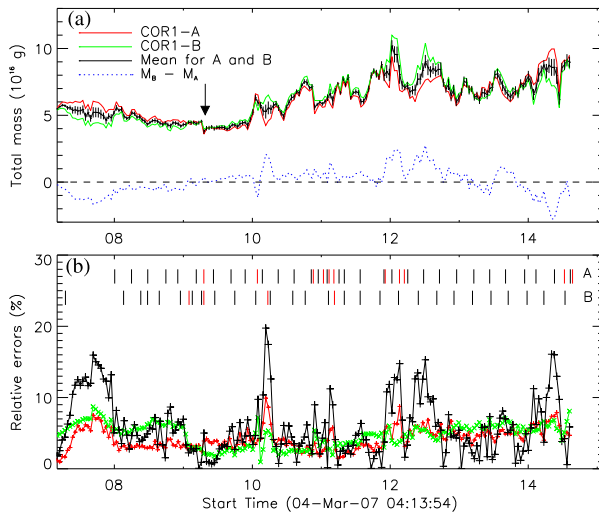


Figure 11 Estimate of errors in the measured total coronal mass from STEREO/COR1. (a) Temporal variations of the total coronal mass integrated from 1.5 to 3.7 R_{\odot} globally (the red line for COR1-A (M_A), the green line for COR1-B (M_B), and the black line for their mean). The error bars are calculated using Equation 3. The dotted curve represents the total mass differences ($M_B - M_A$) between COR1-A and -B. The arrow marks the small drop in total mass when the binning format of COR1 data was changed from 1024×1024 to 512×512 on 19 April 2009. (b) The black curve with the pluses represents the relative mass differences ($|M_B - M_A|/(M_B + M_A)$) between COR1-A and -B, the red curve with the pluses represents the errors (r_{error}^M) for the total coronal mass calculated using Equation 3, and the green curve with the crosses represents the errors (r_{error}^N) for the globally averaged coronal density calculated using Equation 4. Note that the curve r_{error}^N is scaled by a factor of 1/3 for better comparison with r_{error}^M . The thin black bars at the top of panel (b) indicate the times of calibration roll maneuvers for COR1-A (upper row) and COR1-B (lower row) listed in Table 3. The thick red bars indicate the times of the events that cause the COR1 background change listed in Table 4.

($r_{\text{dif}} = |M_A - M_B|/(M_A + M_B)$; see the black line with pluses) have several peaks above 10%. The greatest peak between early 2007 and 2008 results from the absence of calibration rolls during this period, while the other peaks may be involved with the events that affected the COR1 background subtraction (see Table 4). Such events include the spacecraft repoint, the image binning format change, the exposure time change, and the deposition of dust particles on the objective lens (see Thompson *et al.*, 2010). Particularly, the dust landing events caused a sudden jump in the scattered-light background, which was followed by some slight decrease at the beginning. Because the background data were treated separately before and after each event (by calling the routine SCC_GETBKIMG), the background subtraction close to the event did not work well, especially when the combined background with calibration rolls was applied. By comparing these with the results that were recalculated from the 3D density reconstructions made with the pB images processed with the regular monthly minimum backgrounds (see Figure 19 in the Appendix), we confirm that several large peaks in r_{dif} are due to use of calibration roll backgrounds. However, when no calibration roll backgrounds are applied, the total coronal mass is underestimated by $20 \pm 8\%$ on average (see Figure 20 in the Appendix). In addition, the calibration roll background may not work well during solar maximum because of the polar streamers (or absence of CHs). Finally, we note a systematic drop of $\approx 10\%$ in the coronal mass evolution after 19 April 2009 that is due to the change of image binning format (see the arrow marked in Figure 11a). This could be attributed to the alternate way that the data were compressed for telemetering.

Finally, we emphasize that the local spherical symmetry assumption on which the SSPA technique is based, while valid for specific observations (*e.g.* streamer edge-on view), is not valid in general (*e.g.* streamer face-on view). The effect of this situation was demonstrated in Figures 7 and 8 of Wang and Davila (2014), who showed that the SSPA is able to recover the radial electron density profile of a tomographic model of streamers when the favorable viewing conditions are met so that the symmetry in longitude is roughly valid. It was also shown that even in such cases, their matching degree decreases with height as the streamer region takes a progressively smaller part in the LOS. The quantitative comparisons of SSPA reconstructions with the tomographic density model and the MHD density model in this article show that the uncertainty of the SSPA is within a factor of about 2 for most regions where their density ratios are between 1/2 and 2 (see right panels of Figure 5 and Figure 7). These comparisons also show that the SSPA and model densities appear to agree better at greater height. Despite some differences in fine coronal structures between the SSPA and model reconstructions, their globally averaged radial density profiles are consistent (see Figures 6 and 8). This suggests that the spherical symmetry approximation may affect the density reconstruction like a “smoothing” that only causes the redistribution of coronal mass (mainly along longitude), but does not change the total mass. Figure 9 of Wang and Davila (2014) showed such an instance, where the difference in total mass integrated over $1.6\text{--}3.8 R_{\odot}$ between the SSPA inversion and the given density model was about 7%. This smoothing effect can also be verified based on the 2D toy models given in the Appendix of Wang and Davila (2014).

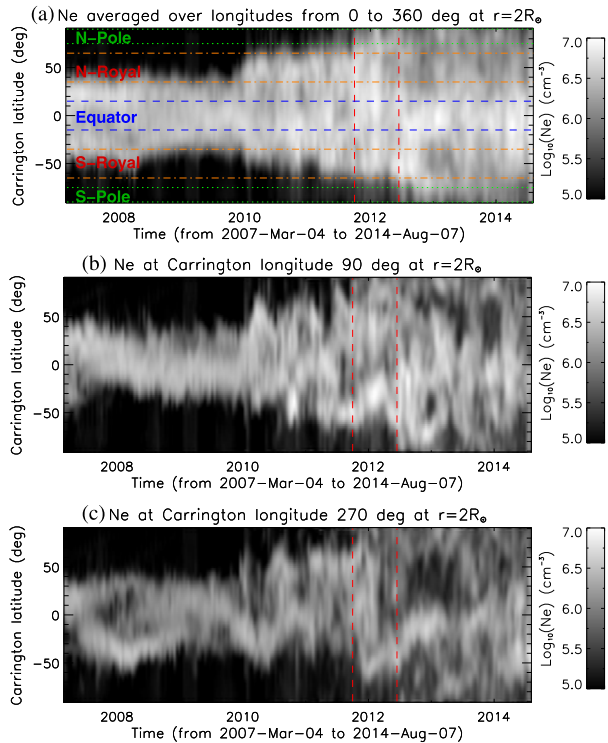
Here we calculated the total mass in the $1.5\text{--}3.7 R_{\odot}$ region using the SSPA and tomographic reconstructions for CR 2066, and obtained $M_{\text{total}}^{\text{SSPA}} = 5.5 \times 10^{16}$ g for COR1-B and $M_{\text{total}}^{\text{tomo}} = 3.9 \times 10^{16}$ g for the tomographic model, where we compared $M_{\text{total}}^{\text{SSPA}}$ for COR1-B with $M_{\text{total}}^{\text{tomo}}$ as the tomographic reconstruction was made of the COR1-B data. We find that the difference between the total mass is $\approx 39\%$, which reduces to only $\approx 10\%$, however, when integrated over the $1.7\text{--}3.7 R_{\odot}$ region. The larger difference in the former case is mainly due to the fault of the tomographic model near the occulter (see Figure 6). We also compared the total mass calculated in $1.5\text{--}3.7 R_{\odot}$ between the SSPA reconstruction and the MHD density model for CR 2097/2098, and find that $M_{\text{total}}^{\text{SSPA}} = 5.3 \times 10^{16}$ g and $M_{\text{total}}^{\text{MHD}} = 5.1 \times 10^{16}$ g, which differ by about 4%. Another caveat can be attributed to the above two examples of SSPA reconstructions, *i.e.* they are made for CRs during solar minimum or the early rising phase, whose density structures during that period are relatively simple and stable. It is known that coronal structures are more complex and dynamic during solar maximum, and therefore a similar analysis of uncertainty for solar maximum rotations (*e.g.* CR 2136 shown in Figure 9) is required in a future study.

4. Coronal Activity

4.1. Long-Term Variations

We used the 3D electron density reconstructions for CRs 2054–2153 to study the temporal evolution of the global corona. Figure 12 shows three time-latitude maps of the electron density, made by stacking in time the longitude-averaged densities (panel (a)), the cut at 90° longitude (panel (b)), and the cut at 270° longitude. The streamer belt is concentrated in the equatorial region during the minimum period of solar activity (from 2007 to 2009), and then expands toward the polar regions as the level of activity increases. Finally, it reaches the polar regions around 2012 and persists globally during the maximum period of solar

Figure 12 Time evolution of latitudinal distributions of the mean electron density for COR1-A and -B at a heliocentric distance of $2 R_{\odot}$. **(a)** averaged over all longitudes, **(b)** along the cut at longitude 90° , and **(c)** along the cut at longitude 270° . Two vertical dashed lines mark the time when streamers reach the North Pole (in October 2011) and the South Pole (in June 2012), respectively. Horizontal lines in **(a)** delineate polar zones (dotted lines), royal zones (dot-dashed lines), and the equatorial zone (dashed lines).



activity (from 2012 to 2014). A careful examination finds that streamers reached the North Pole in October 2011; about eight months earlier than they reached the South Pole. The behavior of the streamer belt is closely related to temporal evolution of the magnetic neutral sheet or the HCS (Schulz, 1973; Guhathakurta, Holzer, and MacQueen, 1996; Saez *et al.*, 2007; Hu *et al.*, 2008). Its shape becomes progressively deformed from a rather flatter plane (concentrated in the equatorial band) around solar minimum to a highly warped surface (reaching high-latitude regions) at solar maximum.

We calculated the total mass of the global corona (M_{total}) from the 3D density reconstructions using Equation 2. By applying $M_{\text{total}} = \mu m_p N_{\text{total}}$, we then derived the globally averaged electron (number) density,

$$N_{\text{mean}} = \frac{N_{\text{total}}}{V_{\text{total}}} = \frac{M_{\text{total}}}{\mu m_p V_{\text{total}}} = C M_{\text{total}}, \tag{5}$$

where N_{total} is the total number of electrons in the analyzed spherical region between $r_1 = 1.5$ and $r_2 = 3.7$, which has the total volume $V_{\text{total}} = (4/3)\pi R_{\odot}^3 (r_2^3 - r_1^3)$, and where the constant $C = 7.5 \times 10^{-12} \text{ cm}^{-3} \text{ g}^{-1}$. As the total mass and the global mean electron density of the corona only differ by a constant factor, their evolution is shown using the same curve (see Figure 13a). Likewise, the calculated total mass and mean electron density in the northern and southern hemispheres are shown in Figures 13b and 13c, respectively. The reason for considering the two hemispheres separately lies in the hemispheric asymmetry of magnetic activity such as the inequality of sunspot numbers (*e.g.* McIntosh *et al.*, 2013; Bisoi *et al.*, 2014; Benevolenskaya, Slater, and Lemen, 2014). In comparison, the total Wolf

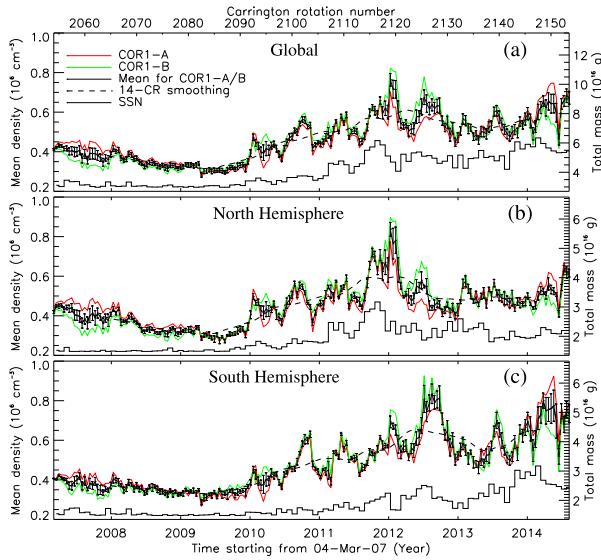


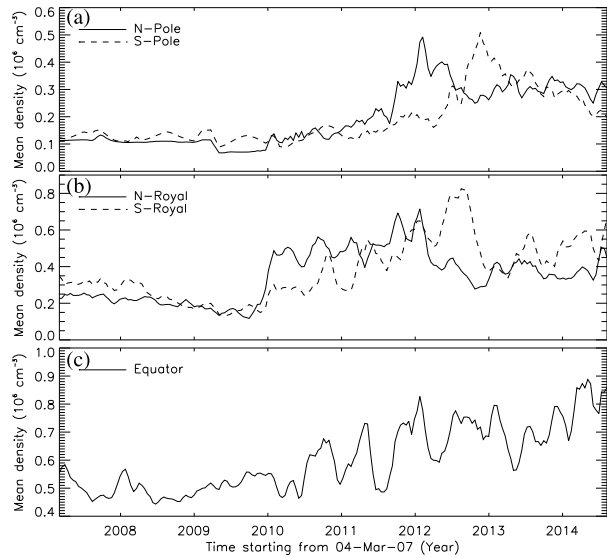
Figure 13 Temporal variations of the electron density in the corona, averaged from 1.5 to $3.7 R_{\odot}$ globally (a), in the northern hemisphere (b), and in the southern hemisphere (c). The red line represents the densities derived from STEREO/COR1-A data, and the green line represents the densities from COR1-B data. The thick black line with the pluses represents the mean densities for COR1-A and -B, and the thick dashed line corresponds to the 14 CR (≈ 13 -month) running average. The thin black line in histogram mode represents the Wolf sunspot numbers (SSN) integrated over each CR (shown in arbitrary unit). The right y-axis indicates the corresponding total coronal mass integrated from 1.5 to $3.7 R_{\odot}$ globally (a), and in hemispheres (b) and (c).

sunspot number (SSN) integrated over each CR is overplotted. The daily total and hemispheric SSN data are publicly available on the WDC-SILSO archive.³

Figure 13 shows that the long-term trend and overlying short-term oscillations of coronal mass variations roughly follow the behavior of the sunspot number, implying dependence on the magnetic activity evolution on the solar surface. The two hemispheres show that the oscillations are clearly out of phase. The measurement shows that the northern oscillation is leading the southern oscillation during the rising phase by ≈ 7 months (eight CRs), based on the time lag between their maxima (reached at about 2012/01 in the northern hemisphere and at 2012/08 in the southern hemisphere). We note that this time lag is close to the time difference for the streamer belt reaching the Northern and Southern Poles. The variability of the K-corona is often characterized by the so-called modulation factors (MFs) that are defined as the ratios between the maximum and minimum of the integrated radiance or pB (e.g. Fisher and Sime, 1984; Barlyaeva, Lamy, and Llebaria, 2015). To determine MFs for the temporal variation of total coronal mass (or mean electron density), we first calculated the 14 CR (≈ 13 -month) running averages that represent the long-term variations (see the dashed lines in Figure 13), and then measured their minimum and maximum values. The 13-month running average is a standard smoothing method, which is widely used (see Hathaway, 2015). We obtained $MF = 1.9$, 1.9 , and 2.0 for the global, the northern and southern hemispheric corona, respectively. The modulation factors indicate that the variation amplitude in the southern hemisphere is slightly larger than in the northern hemisphere.

³<http://sidc.oma.be/silso/datafiles>

Figure 14 Temporal variations in electron density averaged from 1.5 to 3.7 R_{\odot} in different polar regions. **(a)** North and south polar zones. **(b)** North and south royal zones. **(c)** Equatorial zone. All curves in (a)–(c) are calculated as averages for COR1-A and -B, and then smoothed with a two-pixel (1 CR) running average.



Some studies revealed that the hemispheric asymmetry was latitudinally dependent (*e.g.* Bisoi *et al.*, 2014; Barlyaeva, Lamy, and Llebaria, 2015). To analyze this behavior, we defined three latitude regions similar to those in Barlyaeva, Lamy, and Llebaria (2015): the north or south pole in latitude $75^{\circ} - 90^{\circ}$, the north or south high-latitude region from $35^{\circ} - 65^{\circ}$ (also called royal zones, see the definition in Figure 1 of Barlyaeva, Lamy, and Llebaria, 2015), and the equator within latitudes $\pm 15^{\circ}$ (see Figure 12a). We compared the temporal variations of the coronal average density in these regions (see Figure 14) and found that the two royal zones vary with a phase difference that is comparable to the two hemispheres, showing that the northern zone leads the southern zone by ≈ 7 months (a time shift between their maximum peaks). A distinct phase difference is also observed between the two polar zones. We measured a time lag of ≈ 9 months between their maxima (reached at 2012/2 at the North Pole and at 2012/11 at the South Pole). The short-term fluctuations are obvious at the equator during the rising and maximum phases of Cycle 24, but relatively weaker at the poles during this period. From the 14 CR running averages we determined the long-term variations of the average density (or total mass) in different zones in terms of MF. The measured values are listed in Table 2. The modulation factors indicate that the strongest variation is in the polar region, and the weakest is at the equator. In addition, the MF for the southern royal zone is larger than that for the northern royal zone and is consistent with the case for the two hemispheres.

4.2. Variation of Streamers

We analyzed the temporal variations of the total mass in the global corona and in the two hemispheres in the last section. As most of the coronal plasma (or electron content) is concentrated in streamers, the analysis is indeed equivalent for the whole streamers (including the streamer belt and pseudo- and polar streamers). In this section, we analyze the temporal variations of the total area and the average electron density of the whole streamers using the SSPA 3D density reconstructions. We define the streamer region as the location where the densities are above the 3σ noise level. The background noise σ was estimated as the density

Table 2 Modulation factors for the total mass, total area, and average electron density of streamers as defined in the text and calculated from the 14 CR (13-month) running average.

Regions ^a	MF	Regions	MF
Global coronal mass in 3D	1.9	Global coronal mass at 2 R _⊙	2.1
N. hemi. coronal mass in 3D	1.9	N. hemi. coronal mass at 2 R _⊙	2.1
S. hemi. coronal mass in 3D	2.0	S. hemi. coronal mass at 2 R _⊙	2.2
N. pole coronal mass in 3D	4.3	Global streamer area at 2 R _⊙	1.6
S. pole coronal mass in 3D	3.5	N. hemi. streamer area at 2 R _⊙	1.6
N. royal coronal mass in 3D	3.4	S. hemi. streamer area at 2 R _⊙	1.7
S. royal coronal mass in 3D	3.9	Global streamer mean density at 2 R _⊙	1.4
Equator coronal mass in 3D	1.6	N. hemi. streamer mean density at 2 R _⊙	1.5
		S. hemi. streamer mean density at 2 R _⊙	1.5

^aFor 3D regions from 1.5 to 3.7 R_⊙.

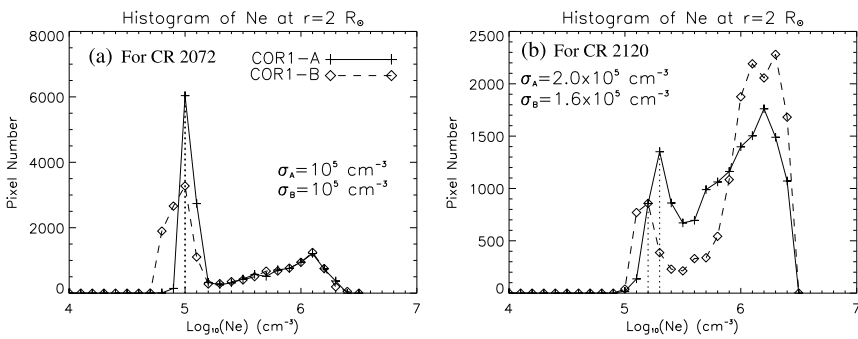
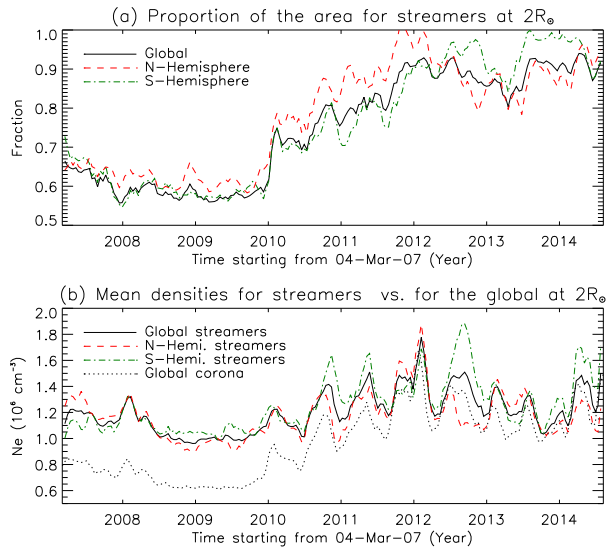


Figure 15 Histograms of the coronal electron densities at a heliocentric distance of 2 R_⊙ for CR 2072 (a) and CR 2120 (b). The solid lines with crosses represent the densities for STEREO/COR1-A, and the dashed lines with diamonds for COR1-B. The background noise (σ) of the 2D density distributions (as shown in Figure 2) is estimated as the density value at the first frequency peak (marked with the vertical dotted lines). The determined noise levels for COR1-A and -B (with σ_A and σ_B) are also marked in the plots.

value at the first peak in the histogram of the densities (in logarithm) created from the spherical cross-sectional density map. Figure 15 illustrates the determination of σ from the density maps at 2 R_⊙ for CR 2072 and CR 2120. The corresponding streamer regions obtained from the 3 σ criteria are shown in Figure 2 (enclosed with the contours). As the background noise only weakly depends on time, we fixed the noise levels at different heights to measure the variation of the streamer regions. The fixed noise levels were taken as the averages over 26 CRs at solar minimum (from CR 2064 to CR 2089). The black solid line (with diamonds) in Figure 17b indicates the radial dependence of the 3 σ noise level averaged for COR1-A and -B.

The measured total areas of streamer regions in the global corona and in the two hemispheres at 2 R_⊙ for CRs 2054–2153 are shown in Figure 16a. The global streamer area increases from below 60% at Cycle 23/24 minimum to above 90% of the whole corona at Cycle 24 maximum. The streamer area in the northern hemisphere is larger than that in the southern hemisphere and is leading in phase during the rising period of solar activity, while it dominates in the southern hemisphere during the maximum phase. From the 14 CR run-

Figure 16 (a) Proportions of the area of the streamer region (with $N_e > 3\sigma$) in the global corona (thick solid line), the northern hemisphere (dashed line) and the southern hemisphere (dot-dashed line) at $2R_\odot$. (b) Temporal variations in average density for the streamer region in the global corona and the two hemispheres. In comparison, the dotted line indicates the globally averaged density (or the total mass) at $r = 2R_\odot$. All curves in (a) and (b) are calculated as the averages for COR1-A and -B, and then smoothed with a two-pixel (1 CR) running average.



ning averages of the time profiles, we measure the modulation factors for the total streamer area to be $MF = 1.6 - 1.7$ (see Table 2). The values for the two hemispheres are very similar. Figure 16b shows temporal variations in average density of the streamer regions in the global corona and in the two hemispheres at $2R_\odot$. We measured the modulation factors from their 14-CR running averages and compared them with those of the globally and hemispherically averaged coronal densities at $2R_\odot$ (equivalent to the total mass; see Section 4.1). These measurements are listed in Table 2. The modulation factors of the latter ($MF = 2.1 - 2.2$) are clearly larger than the former ($MF = 1.4 - 1.5$). This can apparently be explained by the fact that the increase in total coronal mass results from increases in both the total area in 2D (or volume in 3D) and the average density of streamer regions from the minimum to maximum phase. In addition, the modulation factors of the streamer average density in the two hemispheres are very similar. We also find that the oscillations of the streamer average density in the two hemispheres are correlated, and the peaks in the southern hemisphere appear to be larger in amplitude. Finally, it is noted that the oscillation of the streamer average density (thick solid line) is well correlated with that of the globally averaged density (thick dotted line), and that the amplitude of the streamer density oscillation is much larger than that of the streamer area oscillation. These facts may suggest that the oscillations in the global coronal mass (see Figure 13a) are mainly due to the oscillations in the streamer density.

Figures 17a and 17b show the radial dependence of the total area and the average density of streamer regions at solar minimum and solar maximum, respectively. The minimum-phase distributions were calculated by averaging over CRs 2064–2089 and the maximum-phase distributions were calculated by averaging over CRs 2114–2152. The proportion of the total streamer area to the whole spherical area (at the same height) decreases with the radial distance at both solar minimum and maximum, but it appears to decrease faster at minimum than at maximum over the radial distance ranging from $1.5 - 2.0 R_\odot$. The ratio of the total streamer area at solar maximum to that at minimum at the radial distance ranging from $1.5 - 3.7 R_\odot$ is within $1.0 - 2.9$ with a mean of 1.8. We fit the radial profiles of the

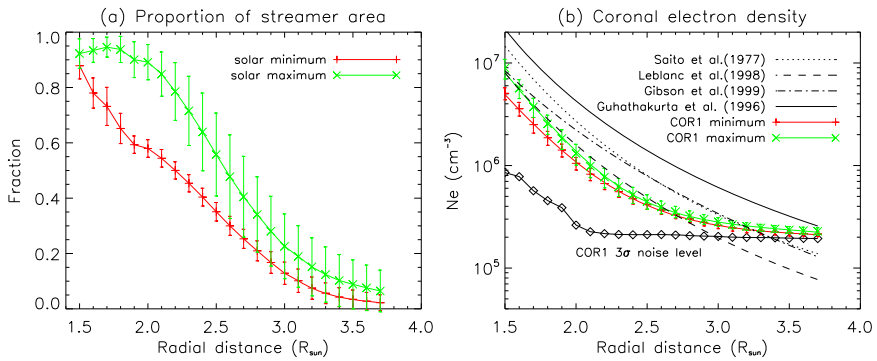


Figure 17 (a) Proportion of the total area of streamer regions (with $N_e > 3\sigma$) in the spherical cross-section of the 3D density as a function of radial distance. The red line with pluses represents the radial distribution averaged over CRs 2064–2089 for both COR1-A and -B during solar minimum, while the green line with crosses represents the average over CRs 2114–2152 for COR1-A and -B during solar maximum. Error bars are the standard deviation for the corresponding average. (b) Radial distributions of the streamer electron density averaged over the areas of $N_e > 3\sigma$ for COR1-A and -B. The red solid line is a least-squares polynomial fit to the radial average densities (denoted with pluses) at solar minimum, while the green solid line is a fit to the radial average densities (denoted with crosses) at solar maximum. The black solid line with diamonds represents the COR1 background noise level (3σ) as a function of radial distance. For comparison, the density models of Saito, Poland, and Munro (1977), Leblanc, Dulk, and Bougeret (1998), Gibson *et al.* (1999), and Guhathakurta, Holzer, and MacQueen (1996) are overplotted as the dotted line, dashed line, dot-dashed line, and the black solid line, respectively.

average streamer density to a fourth-degree polynomial of the form

$$N(r) = \frac{a_1}{r} + \frac{a_2}{r^2} + \frac{a_3}{r^3} + \frac{a_4}{r^4} \quad (1.5 R_\odot \leq r \leq 3.7 R_\odot). \tag{6}$$

We obtained $a_1 = (0.4 \pm 2.0) \times 10^6$, $a_2 = (1.0 \pm 1.6) \times 10^7$, $a_3 = -(5.5 \pm 4.2) \times 10^7$, and $a_4 = (8.2 \pm 3.5) \times 10^7$ for the solar minimum profile ($N(r)_{min}$), and $a_1 = -(4.4 \pm 3.7) \times 10^6$, $a_2 = (5.4 \pm 3.0) \times 10^7$, $a_3 = -(1.9 \pm 0.8) \times 10^8$, and $a_4 = (2.1 \pm 0.7) \times 10^8$ for the solar maximum profile ($N(r)_{max}$). The ratio $N(r)_{max}/N(r)_{min}$ decreases from 1.8 to 1.1 with increasing radial distance from 1.5 to 2.6 R_\odot with a mean of 1.3 in this range. For comparison, Figure 17b also includes the plots for some previous coronal density models obtained at (or near) solar minimum. The dotted curve corresponds to the Saito, Poland, and Munro (1977) density model for the equatorial background (when no streamers or holes were visible), and the dot-dashed curve shows the Gibson *et al.* (1999) density model for streamers. Both density models were obtained from pB observations using the VdH method (Van de Hulst, 1950). The dashed curve is a coronal electron density model derived from radio observations of type III bursts (Leblanc, Dulk, and Bougeret, 1998). We find that $N(r)_{max}$ is consistent with the Leblanc, Dulk, and Bougeret (1998) density model in the 1.5–3.0 R_\odot range. The Saito, Poland, and Munro (1977) density distribution in the 1.5–3.0 R_\odot range is on average larger than $N(r)_{max}$ by a factor of ≈ 1.8 and larger than $N(r)_{min}$ by a factor of ≈ 2.2 . The Gibson *et al.* (1999) density model is in between the Leblanc, Dulk, and Bougeret (1998) and Saito, Poland, and Munro (1977) models. It is noted that the average streamer density $N(r)$ for COR1 distinctly deviates from the Leblanc, Dulk, and Bougeret (1998) density model beyond 3 R_\odot . The reason for the discrepancy is that we defined “streamer regions” as satisfying $N_e > 3\sigma$, where $3\sigma \approx 2 \times 10^5 \text{ cm}^{-3}$ in the range 3.0–3.7 R_\odot . So $N(r)$ can only approach to the 3σ level when decreasing with r , but it will never fall below this value. Thus

it is reasonable to restrict the application range of the obtained density function $N(r)$ to the region $1.5-3.0 R_{\odot}$. In addition, the Guhathakurta, Holzer, and MacQueen (1996) density model (the black solid line) is also overplotted in Figure 17b, which is derived based on the same calibrated data (from *Skylab*) as were analyzed by Saito, Poland, and Munro (1977), but for different coronal structures. The Guhathakurta, Holzer, and MacQueen (1996) density model was obtained at the current sheet (taken as the center or the brightest location of the streamer belt), so the density values may be regarded as an upper limit for streamers. We find that the average density at the current sheet obtained by Guhathakurta, Holzer, and MacQueen (1996) is a factor of 3.6 higher than that of $N(r)_{\min}$ over the range $1.5-3.0 R_{\odot}$ for the streamer region as defined here.

4.3. Short-Term Variations

As mentioned above, the average electron density (or total mass) of the global and hemispheric corona shows clear quasi-periodic oscillations during the rising and maximum phases of Cycle 24. We now analyze these oscillations using the wavelet method (Torrence and Compo, 1998). This method allows us to identify the periodic components in a time series and their variation with time. For the convolution of the time series, we chose the Morlet wavelet. The global wavelet spectrum (GWS) is the average of the wavelet power over time at each oscillation period. Statistically significant oscillation periods are defined

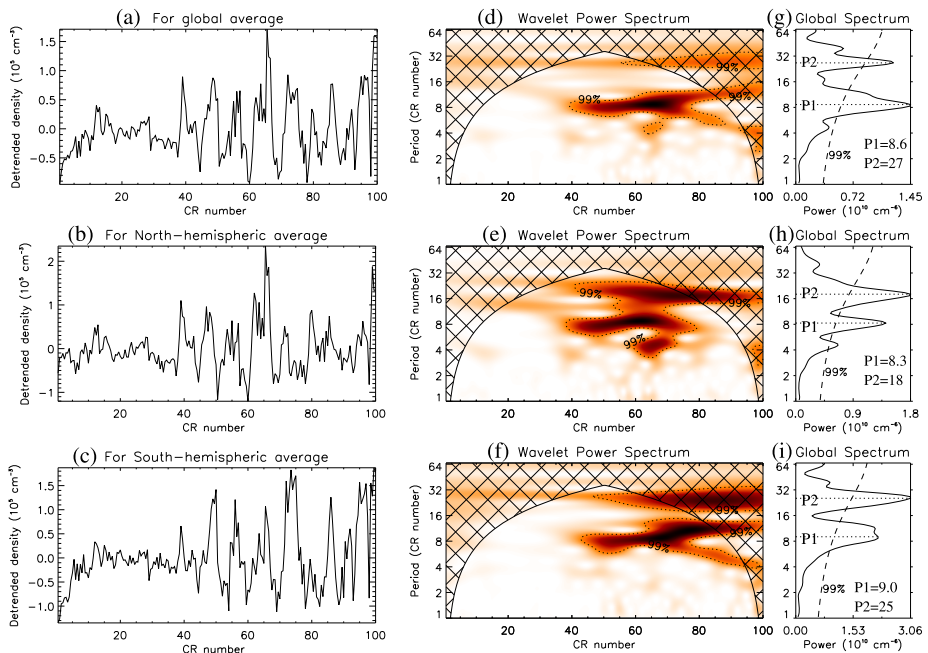


Figure 18 (a)–(c) Detrended electron density variations over the global, north-hemispheric, and south-hemispheric corona, respectively. (d)–(f) Corresponding wavelet power spectra. The dark color represents high power in the power spectra, and the dotted contour encloses regions of greater than 99% confidence. The black grid indicates the region where estimates of the oscillation period become unreliable. (g)–(i) Corresponding global wavelet power spectra. Peaks (in solid line) above the 99% confidence level curve (in dashed line) are statistically significant.

here as exceeding the 99% confidence level against the white-noise background. In practice, we first subtracted the slowly varying long-term trend from the time series. The trend was constructed using Fourier low-pass filtering with a cutoff period of $P_c \gtrsim 20$ CRs. The panels (a)–(c) of Figures 18 show temporal variations of the detrended electron density averaged (for COR1-A and -B) over the region $1.5–3.7 R_\odot$ of the global, north-hemispheric, and south-hemispheric corona, respectively. Panels (d)–(i) show their wavelet analyses. Although two main peaks in the GWS are statistically significant ($> 99\%$ confidence level) (see panels (g)–(i)), the long-period peak ($P_2 = 18–27$ CRs) has power mostly in the “cone of influence” (see panels (d)–(f)), so the estimate of its oscillation period is not reliable because of the edge effects. Thus we determine the period of the short-term oscillations of the corona from the short-period peak ($P_1 = 8–9$ CRs, *i.e.* 7–8 months) in the GWS. Taking the uncertainty of the measurement as the FWHM of the GWS peak, we obtain $P_1 = 9 \pm 3$ CRs for the density variation of the global corona.

5. Discussion and Conclusions

In this study, we reconstructed the 3D electron density models of the corona for CRs 2054–2153 using the SSPA method from STEREO/COR1 pB observations during 2007/3–2014/8. These 3D density reconstructions were validated by comparison with examples of similar models created by other methods such as tomography and MHD simulation and by 2D density distributions inverted using the VdH technique from LASCO/C2 pB images. Some previous studies confirmed that the spherically symmetric inversion (SSI) method was applicable to the solar minimum streamer (belt), which gave coronal densities consistent with those by other techniques such as spectroscopy and tomography within a factor of two (Gibson *et al.*, 1999; Lee *et al.*, 2008; Wang and Davila, 2014). Here we also examined a solar maximum case. By comparing the electron density distributions of CR 2120 (in February 2012) with those inverted from the LASCO/C2 observations, we found that their uncertainties are on the same order (within a factor of two) as in the solar minimum case. This suggests that our SSPA 3D coronal density models reconstructed for 100 CRs (with a cadence of about two weeks) may be used to interpret radio bursts (such as type II and moving type IV produced by CMEs) as observed from the Earth direction (*e.g.* Cho *et al.*, 2007; Ramesh *et al.*, 2013; Shen *et al.*, 2013; Sasikumar Raja *et al.*, 2014; Hariharan *et al.*, 2016; Lee *et al.*, 2016), in particular, when LASCO/C2 pB data are not available. We estimated the total mass (or electron content) contained in the coronal region observed with COR1 and its evolution with the solar cycle. These measurements are important for testing different heating models for magnetic structures in the solar atmosphere (Lionello, Linker, and Mikić, 2009). The error analysis suggests that the effect of CMEs is trivial, while the temporal evolution, instrumental background subtraction, and the spherically symmetric approximation are the main sources of uncertainty in 3D reconstructions of the global corona and estimation of the global coronal mass by the SSPA technique.

We studied the long-term variations of the global and hemispheric corona from solar minimum to the maximum of Cycle 24. A clear hemispheric asymmetry in the evolution of streamers and total coronal mass was found. During the rising phase, the streamer (belt) expands from the equator toward high latitudes. The streamers reach the north pole earlier than the south pole by ≈ 8 months. The variations in coronal mass in the two hemispheres show a similar phase shift (≈ 7 months), with the northern hemisphere leading. The further analysis of the latitudinal dependence of the north-south asymmetry showed that the phase difference between the two poles (≈ 9 months) is similar to that between the two royal

zones (≈ 7 months). In contrast, the measurements for these regions based on variations of the K-coronal radiance using LASCO/C2 were divergent (Barlyaeva, Lamy, and Llebaria, 2015): a time lag of 1 month was found between the two hemispheres, 8 months between the two royal zones, and 17 months between the two poles. The discrepancy between the past results and that in this article may be due to i) different background-subtraction techniques for LASCO/C2 and STEREO/COR1, ii) different definitions for the rising phase of Cycle 24, and iii) different FOVs between C2 and COR1. First, the LASCO/C2 data calibration requires a sophisticated procedure in separating the K corona from the F corona and stray light (see Llebaria, Lamy, and Bout, 2004 and Llebaria, Loirat, and Lamy, 2010, 2012 for details), where the morphology of C2 stray light is invariant during long periods of time, whereas this is not the case for STEREO/COR1 (see Table 4 and Thompson *et al.*, 2010). Our study is based on the COR1 pB data with /CALROLL background subtraction (see Section 3.4). Frazin *et al.* (2012) showed that when used with the /CALROLL option, COR1 pB data matched measurements from LASCO/C2 within streamers well, but the COR1 data were very low in other regions such as CHs. The reason is that the /CALROLL background subtraction method basically takes the CH data as the background level, and thus underestimates the pB. This underestimation affects the entire corona, but is more pronounced in the polar CHs because of their low brightness. The underestimation has a radial dependence, but is insensitive to position angle. Therefore, the underestimation applies equally to the northern and southern hemispheres, and thus should not affect any intercomparison between these two regions. However, the underestimation may become worse during solar maximum as a result of the lack of CHs. This could explain the slight decrease in the measured total coronal mass during this period (see Figure 13). The second reason for the difference between the COR1 and LASCO/C2 results could be that we measured the north-south phase shifts based on the time difference of their largest peaks, while Barlyaeva, Lamy, and Llebaria (2015) used a different technique. For example, we found that the South Pole reaches the maximum at 2012/11, whereas Barlyaeva, Lamy, and Llebaria (2015) determined its maximum at about 2013/05, which corresponds to the second largest peak for the South Pole (see panel D of their Figure 2). In addition, Barlyaeva, Lamy, and Llebaria (2015) did not mention how the hemispheric phase shift was obtained. The third reason could lie in the fact that the total coronal masses for COR1 and C2 were measured by integrating over different radial ranges because of the different FOVs, which may lead to different variations.

Our result agrees with the study of Donner and Thiel (2007), who by a wavelet analysis found that the two hemispheres never shifted out of phase by more than ± 10 months (or 10% of the cycle period) over the past 130 years. Historical sunspot records showed that the northern hemisphere has been leading since about 1965 (the start of Cycle 20), and this hemispheric phase-leading appears to be a secular variation with only several changes occurring during the last 300 years (Zolotova *et al.*, 2010; McIntosh *et al.*, 2013; Hathaway, 2015). Several recent studies suggested that the north-south asymmetry of magnetic activity and the persistent one-hemisphere leading the other may be related to the asymmetry of the meridional flow (McIntosh *et al.*, 2013; Zhao *et al.*, 2013; Virtanen and Mursula, 2014; Blanter *et al.*, 2017). Some nonlinear dynamo models also showed that strong hemispheric asymmetry can be produced by stochastic fluctuations in the dynamo-governing parameters (*e.g.* Mininni and Gómez, 2002, 2004; Usoskin, Sokoloff, and Moss, 2009), or through nonlinear parity modulation (*e.g.* Sokoloff and Nesme-Ribes, 1994; Beer, Tobias, and Weiss, 1998).

The modulation factors are often used to characterize the variability in coronal radiance over solar cycles. Many previous studies determined these factors based on the global K+F corona, the K-corona, or pB observations and found typical values in the range of 2–4

(see Table 1 in Barlyaeva, Lamy, and Llebaria, 2015). The modulation factors vary with the strength of the cycle, but also depend on the way the data are averaged. Using 14-CR (≈ 13 months) running averages, we measured MFs from the increase in total mass (or average electron density) of the corona during the period from minimum to maximum of Solar Cycle 24, and obtained $MF = 1.6-4.3$. This measurement agrees well with Barlyaeva, Lamy, and Llebaria (2015), who obtained $MF_3 = 1.5-4.2$ from the 13-month running average of K-coronal radiance for the same activity period. We found that the modulation factors are latitude dependent, with the largest modulations in the polar regions. This result also agrees with that of Barlyaeva, Lamy, and Llebaria (2015, see Table 3 in their paper). We note that using COR1 data with the /CALROLL background subtraction may lead to an overestimate of the MF, in particular in the polar region, because the radiance is underestimated, as discussed above. However, this effect appears to be trivial as our measured MFs are comparable to those from LASCO/C2. We also found that the modulation factors show a hemispheric asymmetry: MFs in the northern hemisphere and northern royal zone are smaller than in the southern hemisphere and its southern royal zone, but the MF at the North Pole is larger than that at the South Pole. In addition, we measured the variation of streamers, and found that the modulation factors of their total mass depend on the changes in both their total area and average density.

We analyzed the short-term fluctuations of the coronal mass (or coronal electron density) during the rising and maximum epochs of Cycle 24 and determined the oscillation periods to be 8–9 CRs (7–8 months) using a wavelet analysis. The oscillations of the streamer total mass appear to be mainly determined by their mean density oscillations. The periodicities we measured are consistent with those obtained by Barlyaeva, Lamy, and Llebaria (2015) from LASCO/C2 data. Barlyaeva, Lamy, and Llebaria (2015) also found that the oscillation periods over Cycle 23 are about one year and that these quasi-periodic oscillations are highly correlated with those of the photospheric total magnetic flux. Multiple periodicities of solar activity, characterized with variable quasi-periods in the range of 0.6–4 years present in all levels of the solar atmosphere are known as quasi-biennial oscillations (QBOs) (see the comprehensive review by Bazilevskaya *et al.* (2014)). These QBOs are probably linked through the magnetic field, and their origin and periodicities may be associated with stochastic processes of (active region) magnetic flux emergence during the solar cycle (*e.g.* Rieger *et al.*, 1984; Wang and Sheeley, 2003; Hathaway, 2015).

We determined the radial electron density distributions of streamers at solar minimum (from 2007/12 to 2009/10) and maximum (from 2011/8 to 2014/7) of Cycle 24 and found that the average density at solar maximum is only slightly higher (by $\approx 30\%$) than that at solar minimum. This result was not due to the choice of calculating average densities over the areas with $N_e > 3\sigma$. The averages for the streamer regions with $N_e > 1\sigma$ or 6σ give a similar result. By comparison with some previous electron density models of solar minimum such as the Saito, Poland, and Munro (1977) model ($N_{\text{Saito}}(r)$) and the Guhathakurta, Holzer, and MacQueen (1996) model ($N_{\text{GHM}}(r)$) based on observations (1973/5–1974/2) during the declining phase of Cycle 20 near solar minimum, the Leblanc, Dulk, and Bougeret (1998) model ($N_{\text{Leblanc}}(r)$) in the period of 1994/12–1997/11 near the minimum of Cycle 22, and the Gibson *et al.* (1999) model ($N_{\text{Gibson}}(r)$) in 1996/8, our derived solar minimum electron density model ($N(r)_{\text{min}}$) is lowest in value (with average ratios $N_{\text{Leblanc}}/N_{\text{min}} \approx 1.3$, $N_{\text{Gibson}}/N_{\text{min}} \approx 1.8$, and $N_{\text{Saito}}/N_{\text{min}} \approx 2.2$ over 1.5–3.0 R_{\odot}). This can be explained by the fact that this recent solar minimum was observed with a very low solar activity (McIntosh *et al.*, 2013; Bisoi *et al.*, 2014). Lamy *et al.* (2014) showed that the global radiance of the K corona was 24% fainter during minimum of Cycle 23/24 than during that of Cycle 22/23.

De Patoul, Foullon, and Riley (2015) found that the equatorial coronal electron densities obtained using both tomography and a thermodynamic MHD model were lower during 2008–2010 than during 1996–1998. These two studies both support our suggestion. In addition, the significant difference of radial density between different models (*e.g.* $N_{\text{GHM}}/N_{\text{min}} \approx 3.6$) also partially arises from the fact that different features of coronal structures were analyzed.

In conclusion, we studied the long-term and short-term variations of the global K-corona activity in terms of the total coronal mass or mean electron density for Solar Cycle 24. We found a hemispheric asymmetry in both phase and strength: the northern hemisphere leads the southern hemisphere by a shift of 7–9 months, although the former appears to be weaker than the latter, as indicated by the modulation factors. The corona shows a conspicuous quasi-periodicity of 7–8 months during the rising and maximum times. The radial distribution of the mean electron density for streamers at this solar maximum is only slightly larger than at the minimum.

Acknowledgements The work of TW and NLR was supported by the NASA Cooperative Agreement NNG11PL10A to CUA. LASCO was built by a consortium of the Naval Research Laboratory (USA), the Max-Planck-Institut für Sonnensystemforschung (Germany), the Laboratoire d’Astrophysique de Marseille (France), and the University of Birmingham (UK). SOHO is a project of joint collaboration by ESA and NASA. The sunspot data used in this article were obtained from the World Data Center SILSO, Royal Observatory of Belgium, Brussels. We are grateful to the anonymous referee for the constructive comments that improved the manuscript.

Disclosure of Potential Conflicts of Interest The authors declare that they have no conflicts of interest.

Appendix: The STEREO/COR1 Background Subtraction and Its Effect on the Coronal Mass Estimates

Removing instrumental stray light (referred to as background subtraction) is an essential step in the pB data reduction because raw COR1 signals are comprised of three components: the

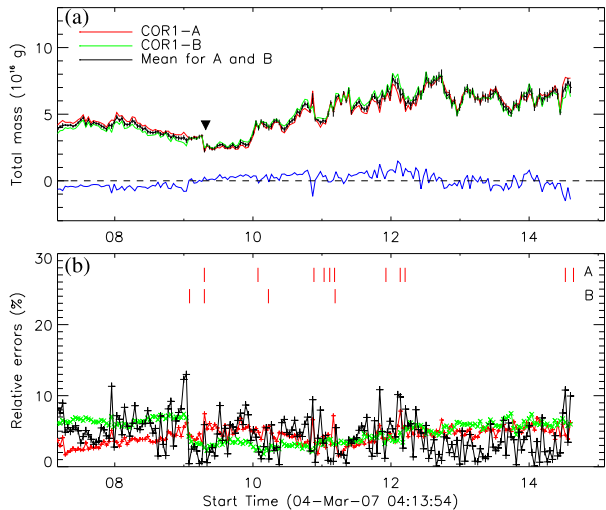
Table 3 Dates for COR1 calibration rolls performed during the period in which the data we analyzed were observed.

	COR1-A	COR1-B	COR1-A	COR1-B
		2007-04-17	2011-04-05	2011-05-03
2008-01-03	2008-02-19	2011-05-03	2011-07-26	
2008-04-01	2008-05-20	2011-07-26	2011-11-08	
2008-06-26	2008-06-25	2011-11-29		
2008-09-30	2008-08-26	2012-01-10	2012-02-14	
2008-12-02	2008-12-16	2012-04-03	2012-05-29	
2009-03-10	2009-02-17	2012-06-26	2012-09-04	
2009-06-09	2009-04-07	2012-09-18	2012-12-04	
2009-09-10	2009-06-16	2012-12-18		
2009-11-24	2009-09-30	2013-03-19	2013-03-12	
2010-02-23	2010-01-19	2013-06-11	2013-06-18	
2010-05-18	2010-04-06	2013-09-03	2013-09-17	
2010-08-10	2010-08-03	2013-12-13	2013-12-26	
2010-11-09	2010-10-08	2014-02-11	2014-03-25	
2010-12-16		2014-05-20	2014-07-15	
2011-02-01	2011-02-08	2014-08-12		

Table 4 Events that significantly changed the COR1 background during the period from 2007/03/04 to 2014/08/07.

Time (UT)	COR1-A events	Time (UT)	COR1-B events
		2009-01-30 16:20	Dust particle landing
2009-04-19 00:00	Change to 512×512	2009-04-19 00:00	Change to 512×512
2010-01-27 16:49	Dust particle landing	2010-03-24 01:17	Dust particle landing
2010-11-19 16:00	Dust particle landing		
2011-01-12 12:23	Dust particle landing		
2011-02-11 04:23	Dust particle landing		
2011-03-08 17:00	Dust particle landing	2011-03-11 18:50	Dust particle landing
2011-12-05 12:03	Dust particle landing		
2012-02-19 02:33	Dust particle landing		
2012-03-16 00:00	Exposure time changing		
2014-07-11 16:00	Dust particle landing		
2014-08-23 17:00	Dust particle landing		

Figure 19 Estimate of uncertainties in the measured total coronal mass from STEREO/COR1 when the pB images are processed with the regular monthly minimum background images. The annotation for all curves is same as Figure 11. The red bars at the top of panel (b) indicate the times of the events that caused a significant change in scattered light background for COR1-A (upper row) and COR1-B (lower row).



K coronal light, the scattered light (weakly polarized), and the F coronal light (unpolarized). The procedures for deriving the time-dependent COR1 instrumental background were described in detail by Thompson *et al.* (2010). Using their methods, two types of background images (namely the monthly minimum backgrounds and the combined monthly minimum and calibration roll backgrounds) are generated every ten days for each of the polarizer settings at 0°, 120°, and 240°. In SSW the routine SECCHI_PREP is used to calibrate the COR1 data, including the process of background subtraction with a choice of using the regular monthly minimum backgrounds by default or using the combined background with the keyword /CALROLL. Table 3 lists the dates for the COR1 calibration roll maneuver during the period of our interest. The comparison of Figure 11 with Figure 19 shows that the differences of the total coronal mass calculated for COR1-A and -B are relatively larger as a result of using the calibration roll backgrounds compared to the case using the regular

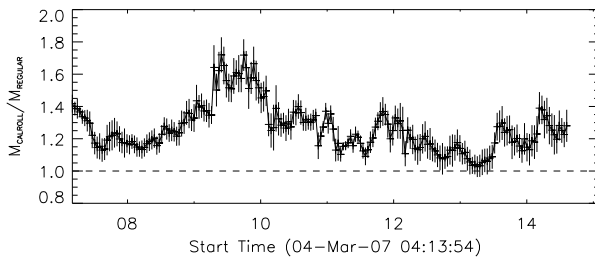


Figure 20 Ratios of the total coronal mass (M_{CALROLL}) measured from the COR1 pB images that are processed with the combined monthly minimum and calibration roll backgrounds to that (M_{REGULAR}) measured from the COR1 pB images that are processed with the regular monthly minimum backgrounds. The error bars are calculated using error propagation rules.

monthly minimum backgrounds. The reason may be that the calibration rolls of COR1-A and -B were performed typically four times a year and were also out of phase, and the calibration roll background images at other times than those listed in Table 3 have to be derived by interpolations (or extrapolations if a background change event occurred between the two closest calibration roll maneuvers). Long-term monitoring reveals that the COR1 background occasionally encounters a sudden increase, which is most likely due to a dust particle landing on the objective lens. For example, the dust landing event on 19 April 2009 for COR1-B is the largest event, and other events that significantly affected the COR1 background are listed in Table 4, where events due to the changes in image binning format and exposure time are also included. However, we caution that the background subtraction close to these events is generally poorer than normal, which may lead to the relatively larger uncertainties in the total coronal mass estimated around these events (see Figure 11b and Figure 19b).

References

- Altschuler, M.D., Newkirk, G.: 1969, *Solar Phys.* **9**, 131. DOI.
- Barbey, N., Guennou, C., Auchère, F.: 2013, *Solar Phys.* **283**, 227. DOI.
- Barlyaeva, T., Lamy, P., Llebaria, A.: 2015, *Solar Phys.* **290**, 2117. DOI.
- Bazilevskaya, G.A., Broomhall, A.-M., Elsworth, Y., Nakariakov, V.M.: 2014, *Space Sci. Rev.* **186**, 359. DOI.
- Benevolenskaya, E., Slater, G., Lemen, J.: 2014, *Solar Phys.* **289**, 3371. DOI.
- Beer, J., Tobias, S.M., Weiss, N.O.: 1998, *Solar Phys.* **181**, 237. DOI.
- Bisoi, S.K., Janardhan, P., Chakrabarty, D., Ananthakrishnan, S., Divekar, A.: 2014, *Solar Phys.* **289**, 41. DOI.
- Blanter, E., Le Mouél, J.-L., Shnirman, M., Courtillot, V.: 2017, *Solar Phys.* **292**, 54. DOI.
- Brueckner, G.E., Howard, R.A., Koomen, M.J., Korendyke, C.M., Michels, D.J., Moses, J.D., *et al.*: 1995, *Solar Phys.* **162**, 357. DOI.
- Charbonneau, P.: 2010, *Living Rev. Solar Phys.* **7**, 3. DOI.
- Cho, K.-S., Lee, J., Moon, Y.-J., Dryer, M., Bong, S.-C., Kim, Y.-H., Park, Y.D.: 2007, *Astron. Astrophys.* **461**, 1121. DOI.
- De Patoul, J., Foullon, C., Riley, P.: 2015, *Astrophys. J.* **814**, 68. DOI.
- Donner, R., Thiel, M.: 2007, *Astron. Astrophys.* **475**, L33. DOI.
- Fisher, R., Sime, D.G.: 1984, *Astrophys. J.* **285**, 354. DOI.
- Freeland, S.L., Handy, B.N.: 1998, *Solar Phys.* **182**, 497. DOI.
- Frazin, R.A., Janzen, P.: 2002, *Astrophys. J.* **570**, 408. DOI.
- Frazin, R.A., Vásquez, A.M., Kamalabadi, F., Park, H.: 2007, *Astrophys. J.* **671**, L201. DOI.
- Frazin, R.A., Lamy, P., Llebaria, A., Vásquez, A.M.: 2010, *Solar Phys.* **265**, 19. DOI.
- Frazin, R.A., Vásquez, A.M., Thompson, W.T., Hewett, R.J., Lamy, P., Llebaria, A., Vourlidis, A., Burkepille, J.: 2012, *Solar Phys.* **280**, 273. DOI.

- Gibson, S.E., Fludra, A., Bagenal, F., Biesecker, D., del Zanna, G., Bromage, B.: 1999, *J. Geophys. Res.* **104**, 9691. DOI.
- Gibson, S.E., Foster, D., Burkepile, J., de Toma, G., Stanger, A.: 2006, *Astrophys. J.* **641**, 590. DOI.
- Guhathakurta, M., Holzer, T.E., MacQueen, R.M.: 1996, *Astrophys. J.* **458**, 817. DOI.
- Hariharan, K., Ramesh, R., Kathiravan, C., Wang, T.J.: 2016, *Solar Phys.* **291**, 1405. DOI.
- Hathaway, D.H.: 2015, *Living Rev. Solar Phys.* **12**, 4. DOI.
- Hayes, A.P., Vourlidis, A., Howard, R.A.: 2001, *Astrophys. J.* **548**, 1081. DOI.
- Howard, R.A., Moses, J.D., Vourlidis, A., Newmark, J.S., Socker, D.G., Plunkett, S.P., et al.: 2008, *Space Sci. Rev.* **136**, 67.
- Hu, Y.Q., Feng, X.S., Wu, S.T., Song, W.B.: 2008, *J. Geophys. Res.* **113**, 3106. DOI.
- Kramar, M., Jones, S., Davila, J.M., Inhester, B., Mierla, M.: 2009, *Solar Phys.* **259**, 109. DOI.
- Kramar, M., Davila, J.M., Xie, H., Antiochos, S.: 2011, *Ann. Geophys.* **29**, 1019. DOI.
- Kramar, M., Airapetian, V., Mikić, Z., Davila, J.M.: 2014, *Solar Phys.* **289**, 2927. DOI.
- Lamy, P., Barlyueva, T., Llebaria, A., Floyd, O.: 2014, *J. Geophys. Res.* **119**, 47. DOI.
- Leblanc, Y., Dulk, G.A., Bougeret, J.-L.: 1998, *Solar Phys.* **183**, 165. DOI.
- Llebaria, A., Lamy, P.L., Bout, M.V.: 2004, In: Fineschi, S., Gummin, M.A. (eds.) *Telescopes and Instrumentation for Solar Astrophysics, Proc. SPIE 5171*, 26. DOI.
- Llebaria, A., Loirat, J., Lamy, P.: 2010, In: Charles, A.B., Ilya, P., Patrick, J.W. (eds.) *Computational Imaging VIII, Proc. SPIE 7533*, 75330Y. DOI.
- Llebaria, A., Loirat, J., Lamy, P.: 2012, In: Clampin, M.R., Fazio, G.G., MacEwen, H.A., Oschmann, J.M. (eds.) *Space Telescopes and Instrumentation 2012: Optical, Infrared, and Millimeter Wave, Proc. SPIE 8442*, 9. DOI.
- Lee, K.-S., Moon, Y.-J., Kim, K.-S., et al.: 2008, *Astron. Astrophys.* **486**, 1009. DOI.
- Lee, J.-O., Moon, Y.-J., Lee, J.-Y., Lee, K.-S., Kim, R.-S.: 2016, *J. Geophys. Res.* **121**, 2853. DOI.
- Linker, J.A., Mikić, Z., Biesecker, D.A., Forsyth, R.J., Gibson, S.E., Lazarus, A.J., et al.: 1999, *J. Geophys. Res.* **104**, 9809. DOI.
- Lionello, R., Linker, J.A., Mikić, Z.: 2009, *Astrophys. J.* **690**, 902. DOI.
- López, F.M., Cremades, M.H., Nuevo, F.A., Balmaceda, L.A., Vásquez, A.M.: 2017, *Solar Phys.* **292**, 6. DOI.
- Mackay, D., Yeates, A.: 2012, *Living Rev. Solar Phys.* **9**, 6. DOI.
- MacQueen, R.M., Burkepile, J.T., Holzer, T.E., Stanger, A.L., Spence, K.E.: 2001, *Astrophys. J.* **549**, 1175. DOI.
- McIntosh, S.W., Leamon, R.J., Gurman, J.B., Olive, J.-P., Cirtain, J.W., Hathaway, D.H., Burkepile, J., Miesch, M., Markel, R.S., Sitongia, L.: 2013, *Astrophys. J.* **765**, 146. DOI.
- Mikić, Z., Linker, J.A., Schnack, D.D., Lionello, R., Tarditi, A.: 1999, *Phys. Plasmas* **6**, 2217. DOI.
- Mikić, Z., Linker, J.A., Lionello, R., Riley, P., Titov, V.: 2007, In: Demircan, O., Selam, S.O., Albayrak, B. (eds.) *Solar and Stellar Physics Through Eclipses, ASP Conf. Ser.* **370**, Astron. Soc. Pac., San Francisco, 299.
- Mininni, P.D., Gómez, D.O.: 2002, *Astrophys. J.* **573**, 454. DOI.
- Mininni, P.D., Gómez, D.O.: 2004, *Astron. Astrophys.* **26**, 1065. DOI.
- Norton, A.A., Charbonneau, P., Passos, D.: 2014, *Space Sci. Rev.* **186**, 251. DOI.
- Ramesh, R., Kishore, P., Mulay, S.M., et al.: 2013, *Astrophys. J.* **778**, 30. DOI.
- Riley, P., Linker, J.A., Mikić, Z., Lionello, R., Ledvina, S.A., Luhmann, J.G.: 2006, *Astrophys. J.* **653**, 1510. DOI.
- Reginald, N.L., Davila, J.M., St. Cyr, O.C., Rastaetter, L.: 2014, *Solar Phys.* 289. DOI. 2021.
- Richardson, I.G., von Rosenvinge, T.T., Cane, H.V.: 2016, *Solar Phys.* **291**, 2117. DOI.
- Rieger, E., Share, G.H., Forrest, D.J., Kanbach, G., Reppin, C., Chupp, E.L.: 1984, *Nature* **312**, 623. DOI.
- Rušin, V., Druckmüller, M., Aniol, P., Minarovjech, M., Saniga, M., Mikić, Z., Linker, J.A., Lionello, R., Riley, P., Titov, V.S.: 2010, *Astron. Astrophys.* **513**, A45. DOI.
- Saez, F., Llebaria, A., Lamy, P., Vibert, D.: 2007, *Astron. Astrophys.* **473**, 265. DOI.
- Saito, K., Poland, A.I., Munro, R.H.: 1977, *Solar Phys.* **55**, 121.
- Sasikumar Raja, K., Ramesh, R., Hariharan, K.C., Kathiravan, C., Wang, T.J.: 2014, *Astrophys. J.* **796**, 56. DOI.
- Schatten, K.H., Wilcox, J.M., Ness, N.F.: 1969, *Solar Phys.* **6**, 442. DOI.
- Schulz, M.: 1973, *Astrophys. Space Sci.* **24**, 371.
- Schrijver, C.J., De Rosa, M.L.: 2003, *Solar Phys.* **212**, 165. DOI.
- Shen, C., Liao, C., Wang, Y., Ye, P., Wang, S.: 2013, *Solar Phys.* **282**, 543. DOI.
- Sokoloff, D., Nesme-Ribes, E.: 1994, *Astron. Astrophys.* **288**, 293. ADS.
- Thompson, W.T., Davila, J.M., Fisher, R.R., Orwig, L.E., Mentzell, J.E., Hetherington, S.E., et al.: 2003, In: Keil, S.L., Avakyan, S.V. (eds.) *Innovative Telescopes and Instrumentation for Solar Astrophysics, Proc. SPIE 4853*, 1. DOI.
- Thompson, W.T., Wei, K., Burkepile, J.T., Davila, J.M., St. Cyr, O.C.: 2010, *Solar Phys.* **262**, 213. DOI.

- Thompson, W.T., Reginald, N.L.: 2008, *Solar Phys.* **250**, 443. [DOI](#).
- Torrence, C., Compo, G.P.: 1998, *Bull. Am. Meteorol. Soc.* **79**, 61. [DOI](#).
- Usoskin, I.G., Sokoloff, D., Moss, D.: 2009, *Solar Phys.* **254**, 345. [DOI](#).
- Van de Hulst, H.C.: 1950, The Electron Density of the Solar Corona. *Bull. Astron. Inst. Neth.* **11**, 135.
- Vibert, D., Peillon, C., Lamy, P., Frazin, R.A., Wojak, J.: 2016, *Astron. Comput.* **17**, 144. [DOI](#).
- Virtanen, I.I., Mursula, K.: 2014, *Astrophys. J.* **781**, 99. [DOI](#).
- Wang, Y.-M., Sheeley, N.R. Jr: 2003, *Astrophys. J.* **590**, 1111. [DOI](#).
- Wang, T.J., Yan, Y., Wang, J.-L., Kurokawa, H., Shibata, K.: 2002, *Astrophys. J.* **572**, 580. [DOI](#).
- Wang, T.J., Davila, J.M.: 2014, *Solar Phys.* **289**, 3723. [DOI](#).
- Zhao, J., Bogart, R.S., Kosovichev, A.G., Duvall, T.L. Jr., Hartlep, T.: 2013, *Astrophys. J. Lett.* **774**, L29. [DOI](#).
- Zolotova, N.V., Ponyavin, D.I., Arlt, R., Tuominen, I.: 2010, *Astron. Nachr.* **331**, 765. [DOI](#).
- Yeates, A.R., Muñoz-Jaramillo, A.: 2013, *Mon. Not. Roy. Astron. Soc.* **436**, 3366. [DOI](#).